FGFR3 Alterations in Bladder Cancer Stimulate Serine Synthesis to Induce Immune-Inert Macrophages That Suppress T-cell Recruitment and Activation

Yi Ouyang[1,2,3], Ziwei Ou[1,2,3], Wenlong Zhong[1,2,3], Jin Yang[4], Sha Fu[5], Nengtai Ouyang[5], Junyu Chen[1,2,3], Longhao Xu[1,2,3], Daqin Wu[1,2,3], Junan Qian[6], Yi Lin[1,2,3], Tianxin Lin[1,2,3], and Jian Huang[1,2,3]

ABSTRACT

FGFR3 alterations are common in patients with bladder cancer. While the FGFR tyrosine kinase inhibitor erdafitinib has been approved as a targeted therapy for patients with *FGFR3*-altered (a*FGFR3*) bladder cancer, the response rate remains suboptimal, prompting development of strategies to improve treatment response. Here, we observed an immune-desert tumor microenvironment (TME) phenotype in human a*FGFR3* bladder cancer and demonstrated that mutant *FGFR3* indirectly induces a "cold" TME in mouse bladder cancer models. Single-cell RNA sequencing revealed the central role of macrophages in inducing the cold TME of a*FGFR3* tumors. Macrophages in a*FGFR3* tumors exhibited reduced T-cell recruitment and antigen presentation capabilities. Increased serine synthesis in bladder cancer cells that was induced by mutant *FGFR3* activated the PI3K/Akt pathway in macrophages, shifting them to an immune-inert phenotype. Targeting PI3K in a*FGFR3* tumors with duvelisib achieved promising efficacy by reversing the macrophage phenotype, and combination therapy with duvelisib and erdafitinib demonstrated increased antitumor activity. Overall, these findings reveal the critical role of enhanced serine synthesis efflux from cancer cells with mutant FGFR3 in shifting macrophages to an immune-inert phenotype. Reversing the macrophage phenotype holds promise for enhancing erdafitinib efficacy.

Significance: Metabolic reprogramming of bladder cancer cells driven by mutant *FGFR3* increases serine synthesis that suppresses macrophage immunostimulatory functions to generate an immunosuppressive TME, which can be overcome by targeting PI3K.

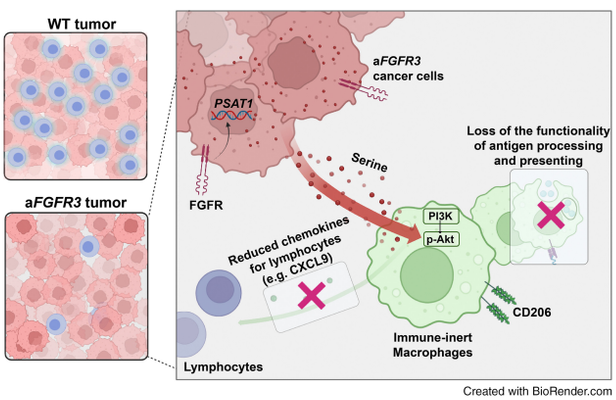

Introduction

Bladder cancer is one of the most common cancers worldwide (1). Platinum-based chemotherapy has traditionally been the standard of care for advanced bladder cancer, but the development of new therapies has led to the emergence of combination therapies that offer improved outcomes, including antibody–drug conjugate, immune checkpoint inhibitors (ICI), and erdafitinib for patients with alterations to *FGFR* (2). Previous research has shown that 17%–32% of bladder cancer harbors *FGFR* family alterations (including *FGFR* mutations, amplifications, and fusions), especially in early-stage disease (3, 4). *FGFR3* alteration is the most common *FGFR* alteration in bladder cancer, accounting for approximately 47.5% of all *FGFR* alterations (5, 6). Nevertheless, the efficacy of erdafitinib, the pan-FGFR inhibitor and the only targeted drug approved by the FDA for bladder cancer, is only approximately 40% in patients with bladder cancer with *FGFR* alterations, indicating an urgent need for new therapies for erdafitinib nonresponders (7).

Traditionally, *FGFR* alterations were believed to solely promote cancer cell proliferation and survival (8). However, recent studies have suggested that *FGFR* alterations are also strongly associated with deleterious immune microenvironments. For example, *FGFR* alterations are associated with the luminal or luminal-papillary subtype, which is characterized by low $CD8^+$ T-cell infiltration (9, 10). One study indicated that *FGFR* alterations facilitate bladder tumorigenesis by inhibiting acute inflammation (11). Others have shown that PD-L1 could be upregulated by *FGFR* activation in cancer cells through various pathways, leading to inactivation of T cells (12–14). Nonetheless, more efforts are needed to elucidate the association between *FGFR* activation and the deleterious tumor microenvironment (TME).

[1]Department of Urology, Sun Yat-sen Memorial Hospital, Sun Yat-sen University, Guangzhou, P.R. China. [2]Guangdong Provincial Key Laboratory of Malignant Tumor Epigenetics and Gene Regulation, Sun Yat-sen Memorial Hospital, Sun Yat-sen University, Guangzhou, P.R. China. [3]Guangdong Provincial Clinical Research Center for Urological Diseases, Guangzhou, P.R. China. [4]Clinical Medical College & Affiliated Hospital of Chengdu University, Chengdu University, Chengdu, Sichuan, P.R. China. [5]Cellular & Molecular Diagnostics Center, Sun Yat-sen Memorial Hospital, Sun Yat-sen University, Guangzhou, P.R. China. [6]Department of Urology, Yan'an Hospital, Kunming Medical University, Kunming, P.R. China.

Y. Ouyang, Z. Ou, and W. Zhong contributed equally to this article.

Corresponding Authors: Jian Huang, Sun Yat-sen Memorial Hosptial, Sun Yat-sen University, 107 Yanjiangxi Road, Guangzhou, Guangdong 510120, P.R. China. E-mail: huangj8@mail.sysu.edu.cn; Tianxin Lin, lintx@mail.sysu.edu.cn; and Wenlong Zhong, zhongwlong3@mail.sysu.edu.cn

Cancer Res 2023;83:4030–46

doi: 10.1158/0008-5472.CAN-23-1065

Metabolic reprogramming, one of the major hallmarks of cancers, has often been observed in cancer cells with oncogenic activation, such as FGFR family mutations (15). Studies have suggested that various oncogenes orchestrate metabolic reprogramming by inducing broad changes in gene expression (16). The Warburg effect is a well-known instance of metabolic rewiring in cancer, whereby cancer cells obtain surplus glycolytic intermediates utilized as inputs for a range of biosynthetic pathways (17). The significance of serine synthesis and metabolism in cancer cells has been emphasized in recent years as an auxiliary pathway of the Warburg effect, owing to its critical role in tumor progression. This metabolic pathway provides essential precursors for protein synthesis, influences the cellular antioxidative capacity, provides methyl groups for the one-carbon pools, and supports tumor homeostasis (18). Studies have suggested that cancer cell–derived serine promotes the development of a supportive tumor immune microenvironment. For instance, serine supplementation decreased the secretion of inflammatory cytokines from macrophages, including IL1β, IFNγ, and TNFα (19, 20). In addition, the enzyme phosphoglycerate dehydrogenase (PHGDH), which was essential for serine synthesis, was found to be a metabolic checkpoint of macrophage differentiation, and it was essential for the expression of key anti-inflammatory molecules (21). However, the underlying mechanism by which cancer cell–derived serine affects the surrounding immune and stromal cells has rarely been studied.

In this study, we discovered that increased serine synthesis derived from *FGFR3*-mutant (m*FGFR3*) cancer cells shifted macrophages to an immune-inert phenotype and elicited a cold TME. We revealed the mechanistic connections among *FGFR3* alterations, serine metabolism, and antitumor immunity and further demonstrated that redirecting the macrophage phenotype with PI3K inhibitors is a potential therapeutic approach for m*FGFR3* tumors.

Materials and Methods

The key resources and reagents used in this study are summarized in Supplementary Table S1. Methods regarding cancer cell supernatants preparation, mouse lymphocytes preparation, lymphocyte coculture assay, tumor-infiltrating lymphocyte classification, cell viability tests, Sun Yat-sen Memorial Hospital (SYSMH) cohort generation, and PSAT1 IHC evaluation were summarized in the Supplementary Materials and Methods.

Cells

The human bladder cancer cell line T24 and human monocyte cell line THP-1 were obtained from the ATCC. The murine breast cancer cell line MB49 was obtained from Millipore. The cells were grown according to standard protocols. Short tandem repeat authentication of the cells used in this study showed that there was no misidentification or contamination with other cells within 3 years. Cell lines were tested for *Mycoplasma* monthly using the Mycoplasma Detection Kit (catalog no. rep-mys-20, InvivoGen) and used within 10 passages.

Animals

All animal experiments were performed with the approval of the Institutional Animal Care and Use Committee (IACUC) of the South China University of Science and Technology (approval number 2022044) and according to the established guidelines. C57BL/6J mice and BALB/c nude mice used in this study were between 4 and 6 weeks old and purchased from Hunan Silaikejingda Experimental Animal Company Limited. huPBMC-NOG-dKO humanoid mice were purchased from Beijing Vital River Animal Company Limited. All mice were maintained in the South China University of Technology (Guangzhou, P.R. China) animal facility under specific pathogen-free conditions.

Lentivirus generation and gene transfer

The entire process of lentiviral construction and generation was entrusted to IGE Biotechnology. In brief, the cDNA sequence encoding human or mouse wild-type (WT) *FGFR3b* was cloned into the pCDH-CMV-MCS-EF1-copGFP-T2A-Puro vector and served as a template for site-directed mutagenesis. The activating mutation S249C (human) or S243C (mouse) was introduced into the *FGFR3b* cDNA by PCR using primers carrying the mutations, which was confirmed by sequencing. Lentiviral vectors encoding no insert or mutant human or mouse *FGFR3b* were transfected into HEK293T cells for packaging. Packaged lentivirus particles were collected from HEK293T cell supernatant and transduced into T24 or MB49 cells in the presence of polybrene (IGE Biotechnology). Successful infection was confirmed by the identification of green fluorescent cells. Infected cells were selected using increasing doses of puromycin (catalog no. 0219453925, MP). Successful infection was confirmed by the identification of green fluorescent cells, qRT-PCR, and Western blotting.

Preparation and culture of bone marrow–derived macrophages

Bone marrow cells were flushed from the femurs and tibias of 6 to 8 weeks old C57BL/6 mice. The erythrocytes were lysed with red blood cell lysis buffer (catalog no. CW0613S, CWBio). The remaining cells were seeded into 6-well or 12-well plates. Bone marrow–derived macrophages (BMDM) were cultured in DMEM supplemented with 10% FBS, 1% penicillin/streptomycin (Gibco), and 40 ng/mL murine MCSF (catalog no. 51112-MNAH, Sino Biological). Fresh culture medium was added to BMDMs every 3 days. On the 6th day of differentiation, the BMDMs were considered matured for *in vitro* stimulation.

Macrophages stimulation assay

Mature BMDMs were cocultured with tumor cell-conditioned medium for 48 hours and harvested for flow cytometry, qRT-PCR, or functional assays. Serine (2 mmol/L; catalog no. BS932, Biosharp), S-Adenosyl methionine (SAM, 1 mmol/L, Sigma-Aldrich, A7007), duvelisib (20 μmol/L; catalog no. A1720, APExBIO), or L-phenylglycine (50 μmol/L; catalog no. 2935-35-5, Sigma-Aldrich) was added. Lipopolysaccharide (100 ng/mL; catalog no. BS904, Biosharp) or murine IL4 (20 ng/mL; catalog no. 214-14-20, Peprotech) was added 24 hours before harvesting to induce proinflammatory or anti-inflammatory macrophages.

Transwell assay

For the transwell assay, 3×10^5 cancer cells or 5×10^5 stimulated macrophages were seeded into the bottom chamber (wells in a 24-well plate) with 500 μL DMEM containing 10% FBS. Next, 5×10^5 lymphocytes were added into the upper chamber (5-μm transwell inserts, catalog no. 3421-48EA, Corning) with 200 μL serum-free media. After 2.5 hours, the number of migrated lymphocytes was quantified by flow cytometry.

Antigen-presenting assay

A total of 5×10^5 BMDMs were cultured with cancer cell supernatants for 48 hours. Then, the cells were incubated with ovalbumin (OVA; 1 μg/mL, catalog no. 9006-59-1, Solarbio) for 24 hours. The cells were collected, washed with PBS, and stained with PE anti-mouse H-2Kb

bound to SIINFEKL antibody (catalog no. 12-5743-81, Thermo Fisher Scientific, RRID: AB_925775) in PBS at 4°C for 1 hour.

RNA sequencing and *in silico* analysis

Public transcriptional databases and immune infiltration analysis

Transcriptome and clinical data in the IMvigor210 dataset obtained from patients with metastatic urothelial bladder cancer treated with atezolizumab were downloaded from http://research-pub.gene.com/IMvigor210CoreBiologies. The Cancer Genome Atlas (TCGA)-BLCA dataset was extracted from TCGA and used for further analyses. We integrated gene set enrichment analysis (GSEA) to estimate immune infiltration, and the signature used in this study is summarized in Supplementary Table S2.

Single-cell RNA sequencing of mouse MB49 tumor samples

A total of six samples (three per group) were used for single-cell RNA sequencing (scRNA-seq), and the samples of each group were mixed before sequencing. Droplet-based sequencing data from Singleron Matrix Single Cell Processing System was aligned and quantified against the mm10 mouse reference genome using CeleScope (https://github.com/singleron-RD/CeleScope) v1.9.0 pipeline. Seurat version 4.2.0 was used for cell filtering and subsequent analysis (22). The filtered data were normalized using a normalized data function with a scaling factor of 10,000. The top 2,000 highly variable genes were selected using the "find variable feature" function in the first method. Mutual nearest neighbors were used to remove the batch effects (23). FindNeighbors and FindClusters functions were employed with 10 dimensions and a resolution of 0.8. We used CellChat (1.1.0), a public repository of ligands, receptors, cofactors, and their interactions, for the inference and analysis of cell-to-cell communication. For the macrophage subcluster analysis, FindNeighbors and FindClusters functions were employed with five dimensions and a resolution of 0.3. GSEA (RRID: SCR_003199) was applied to identify significantly enriched pathways using the GSEA 4.1.0 desktop application.

qRT-PCR

Total RNA was extracted from macrophages and MB49 or T24 cancer cells using an RNA Quick Purification Kit (EZBioscience). qRT-PCR was performed using HieffTM qPCR SYBR Green Master mix (Yeasen Biotechnology) and analyzed using a LightCycler 480 instrument (Roche). The primer sequences are listed in Supplementary Table S3.

Serine quantification assay

We used a DL-Serine Assay Kit (catalog no. MAK352, Sigma-Aldrich) according to the manufacturer's instructions to analyze the relative serine concentration within cancer cells and BMDMs.

Western blotting

Conditioned cells were lysed using RIPA lysis buffer (catalog no. CW2333S, CWBio) in the presence of protease inhibitors (catalog no. CW2200S, CWBio) and phosphatase inhibitors (catalog no. CW2383S, CWBio). Proteins were quantified using a bicinchoninic acid assay (catalog no. CW0014S, CWBio) before denaturation. Protein samples were then subjected to SDS-PAGE and transferred to polyvinylidene difluoride membranes (catalog no. IPVH00010, Merck Millipore), which were blotted with anti-pERK1/2 (diluted 1:2,000, catalog no. 4370, Cell Signaling Technology, RRID: AB_2315112), anti-pERK5 (diluted 1:1,000; catalog no. 3371, Cell Signaling Technology, RRID: AB_2140424), anti-PSAT1 (diluted 1:5,000; catalog no. 10501-1-AP, Proteintech, RRID: AB_2172597), and anti-α-tubulin (diluted 1:20,000; catalog no. 66031-1-Ig, Proteintech, RRID: AB_11042766) antibodies, followed by incubation with horseradish peroxidase–conjugated anti-rabbit secondary antibodies (catalog no. GB23303, Servicebio) or anti-mouse secondary antibodies (catalog no. GB23303, Servicebio). Membrane proteins were visualized using SmartChemi 910 plus (Beijing Sage Creation Science Co, LTD) utilizing chemiluminescence (catalog no. WBKLS0500, Merck Millipore).

Flow cytometry of *in vitro* experiments

BMDMs were harvested for flow cytometry after the coculture assay as described above and blocked with mouse Fc Receptor Blocking Solution (catalog no. 101320, BioLegend, RRID: AB_1574975) before incubation with fluorochrome-labeled antibodies. The antibodies used for BMDM surface staining were BV510 anti-F4/80 (catalog no. 123135, BioLegend, RRID: AB_2562622), PE-Cy7 anti-CD11b (catalog no. 101215, BioLegend, RRID: AB_312798), and BV605 anti-IA/IE (catalog no. 107639, BioLegend, RRID: AB_2565894). A FIX & PERM Cell Permeabilization Kit (catalog no. GAS003, Thermo Fisher Scientific) was used to fix and permeabilize the cell membranes. The BMDMs were then incubated with Fixation Medium for 15 minutes, washed, and incubated Permeabilization Medium and PE anti-CXCL9 (catalog no. 515603, BioLegend, RRID: AB_2245490), PE anti-pAKT1 (catalog no. 12-9715-41, Thermo Fisher Scientific, RRID: AB_2637101), or AF647 anti-CD206 (catalog no. 141711, BioLegend, RRID: AB_10900240) antibodies for intracellular staining.

THP-1 cells were also harvested for flow cytometry after the coculture assay as described above and blocked with human Fc Receptor Blocking Solution (catalog no. 422302; BioLegend, RRID: AB_2818986). The PE anti-HLA-DR antibody (catalog no. 307605, BioLegend, RRID: AB_314683) was used for THP-1 surface staining. THP-1 cells were fixed and permeabilized as described above and incubated with BV421 anti-Human CD206 (catalog no. 566281, BD Biosciences, RRID: AB_2739655), or PE anti-CXCL9 (catalog no. 566013, BD Biosciences, RRID: AB_2739458) antibodies for intracellular staining.

Flow cytometry was performed using a CytoFLEX flow cytometer (Beckman Coulter) and analyzed using FlowJo (version 10, RRID: SCR_008520).

IHC

Formalin-fixed paraffin-embedded tumor tissues isolated were cut into 5-μm sections and used for IHC staining. For humanized tumor tissues, IHC staining of CD206 (diluted 1:1,500; catalog no. 24595, Cell Signaling Technology, RRID: AB_2892682) and CD8 (diluted 1:500; catalog no. MA5-14548, Thermo Fisher Scientific, RRID: AB_10984334) was performed. IHC staining for CXCL9 (diluted 1:1,000; catalog no. AF-492-NA, R&D Systems, RRID: AB_2086734) was performed for mouse tumor tissues. IHC staining for PSAT1 (diluted 1:200; catalog no. 10501-1-AP, Proteintech, RRID: AB_2172597) was performed in human bladder cancer tissues from the SYSMH cohort. Details of IHC were summarized in the Supplementary Materials and Methods.

Multicolor immunofluorescence

Multiplex immunofluorescence (IF) was performed using a PANO 5-plex IHC kit (catalog no. 10080100100, PANOVUE). The primary antibodies used for multiplex IF staining of mouse tumor tissues consisted of anti-F4/80 (diluted 1:3,000; catalog no. 70076, Cell Signaling Technology, RRID: AB_2799771); anti-CD206 (diluted 1:3,000; catalog no. 24595, Cell Signaling Technology,

RRID: AB_2892682); anti-CD8 (diluted 1:1,200; catalog no. 98941, Cell Signaling Technology, RRID: AB_2756376); anti-granzyme B (diluted 1:2,000; catalog no. 46890, Cell Signaling Technology); and PE anti-IA/IE antibodies (diluted 1:200; catalog no. 107607, BioLegend, RRID: AB_313322). For human bladder cancer tissue staining, anti-CD68 (diluted 1:1,000; catalog no. ZM-0464, Zhongshan Golden Bridge); anti-HLA-DR (diluted 1:2,000; catalog no. ZM-0136, Zhongshan Golden Bridge); anti-CD206 (diluted 1:3,000; catalog no. 24595, Cell Signaling Technology, RRID: AB_2892682); anti-CXCL9 (diluted 1:1,000; catalog no. ab202961, Abcam); anti-CD8 (diluted 1:3,000; catalog no. MA5-14548, Thermo Fisher Scientific, RRID: AB_10984334); anti-granzyme B (diluted 1:1,000, catalog no. 46890, Cell Signaling Technology) was used. For primary antibodies without a fluorescent label, after incubation with the primary and secondary antibodies (catalog nos. MP-7451 and MP-7444, Vector), the sections were stained with Alexa Fluor Tyramides Opal 520, 570, 620, or 690 following the manufacturer's instructions. Finally, the slides were counterstained with DAPI, mounted with an anti-fade mountant, and scanned using the Vectra Polaris Automated Quantitative Pathology Imaging System (PerkinElmer). The evaluation was performed using Phenochart and inForm Tissue Analysis software (PerkinElmer). Alexa Fluor Tyramides, DAPI, and anti-fade mountant were all included in the kit.

Animal experiments

For the humanized mouse experiment, T24 cells (5×10^6) were implanted subcutaneously into the right flank. In other animal experiments, MB49 cells (5×10^5) were inoculated subcutaneously for the subcutaneous tumorigenicity assay. The tumor diameter was monitored every 2–3 days using an electronic caliper. Tumor volumes were calculated as $0.5 \times L \times W^2$.

For the macrophage depletion study, neutral clodronate liposomes (catalog no. F70101C-N, FormuMax, 7 mg/mL, 200 μL, intraperitoneal) and control liposomes (catalog no. F70101-N, FormuMax, 200 μL, intraperitoneal) were given on the second, sixth, 10th, and 14th day after cell inoculation. Tumors were harvested on the 16th day.

For the duvelisib treatment study, from the 10th day after tumor cell inoculation, mice were injected with duvelisib (catalog no. A1720, APExBIO, 2 mg/kg, oral gavage) every day. For the erdafitinib treatment study, from the 10th day after tumor cell inoculation, the mice were injected with erdafitinib (catalog no. JNJ-42756493, MCE, 25 mg/kg, oral gavage) every day. Mice in the control group received vehicle treatment.

Flow cytometry for animal experiments

Antibodies were purchased for the animal experiment flow cytometric analyses, including Brilliant Violet 650 anti-CD8α (catalog no. 100741, BioLegend, RRID: AB_11124344); PE anti-CD3 (catalog no. 100206, BioLegend, RRID: AB_312663); PE/Cyanine7 anti-CD4 (catalog no. 100421, BioLegend, RRID: AB_312706); Alexa Fluor 647 anti-granzyme B (catalog no. 515406, BioLegend, RRID: AB_2566333); PE anti-CXCL9 (catalog no. 515603, BioLegend, RRID: AB_2245490); Brilliant Violet 605 anti-IA/IE (catalog no. 107639, BioLegend, RRID: AB_2565894); Brilliant Violet 510 anti-F4/80 (catalog no. 123135, BioLegend, RRID: AB_2562622); PE/Cyanine7 anti-CD11b (catalog no. 101215, BioLegend, RRID: AB_312798); and Brilliant Violet 421 anti-CD45 (catalog no. 103134, BioLegend, RRID: AB_2562559).

Tumor-bearing mice were euthanized at designated timepoints, and their tumors were isolated and stored in ice-cold 2% FBS. The collected tumors were then minced into 1–3 mm pieces using a scalpel before incubation with collagenase I (catalog no. GC305013, Servicebio), collagenase II (catalog no. GC305014, Servicebio), collagenase IV (catalog no. GC305015, Servicebio), and DNase (catalog no. 1121MG010, Servicebio) for 1 hour at 37°C on a shaker. The resulting tumor suspensions were then passed through a 40-μm cell strainer to remove large debris and generate single-cell suspensions.

Macrophage surface staining was performed by incubating 1×10^6 cells in 50 μL ice-cold PBS with fluorochrome-conjugated antibodies against CD45, CD11b, F4/80, and IA/IE. The cells were then washed again with PBS, fixed, permeabilized as described above, and stained using an intracellular anti-CXCL9 antibody.

Lymphocyte surface staining was performed by incubating 1×10^6 cells in 50 μL ice-cold PBS with fluorochrome-conjugated antibodies against CD3, CD4, CD45, and CD8. The cells were then washed again with PBS, fixed, permeabilized as described above, and stained using an intracellular anti-granzyme B antibody.

Statistical analysis and data presentation

All experiments in this study were independently performed three times. Quantitative data are presented as the mean ± SEM. The χ^2 test was used for nonparametric variables, while Student *t* test and one-way ANOVA were used for parametric variables to identify statistically significant data. All data analyses were performed using GraphPad Prism version 9 (RRID: SCR_002798). A P value < 0.05 was considered to indicate significance. The proposed illustration of mechanism and experiments was created with BioRender.com.

Study approval

All human samples used in this study were obtained from patients with their written informed consent. The study was conducted in accordance with the Declaration of Helsinki and was approved by the Ethics Committee of the Sun Yat-sen Memorial Hospital, Sun Yat-sen University (approval number SYSKY-2023-422-01). The baseline information of patients included in the cohort was summarized in Supplementary Table S4. All animal experiments were performed with the approval of the IACUC of the South China University of Science and Technology (approval number 2022044).

Data availability statement

The IMvigor210 dataset analyzed in this study was downloaded from http://research-pub.gene.com/IMvigor210CoreBiologies. In addition, TCGA-BLCA cohort data analyzed in this study was extracted from TCGA at https://www.cancer.gov/ccg/research/genome-sequencing/tcga. The scRNA-seq data that support the findings of this study have been deposited into the Gene Expression Omnibus with accession number GSE243093 and the CNGB Sequence Archive (CNSA) of China National GeneBank DataBase (CNGBdb) with accession number CNP0004744. Other data supporting the findings of this study are available upon request from the corresponding author.

Results

FGFR3-altered bladder cancers indirectly shape a cold TME

FGFR3-altered (a*FGFR3*) bladder cancer has previously been reported to be associated with a non–T-cell–inflamed TME. We conducted a systematic review utilizing publicly available databases IMvigor210 and TCGA-BLCA to comprehensively assess the immune infiltration of a*FGFR3* bladder cancer tumors (24). First, we utilized a previously established $CD8^+$ effector T-cell signature to evaluate the infiltration level of $CD8^+$ T cells (25). Our analysis revealed a significant decrease in the infiltration of $CD8^+$ T cells in the a*FGFR3* bladder cancer group compared with that in the WT group (**Fig. 1A**).

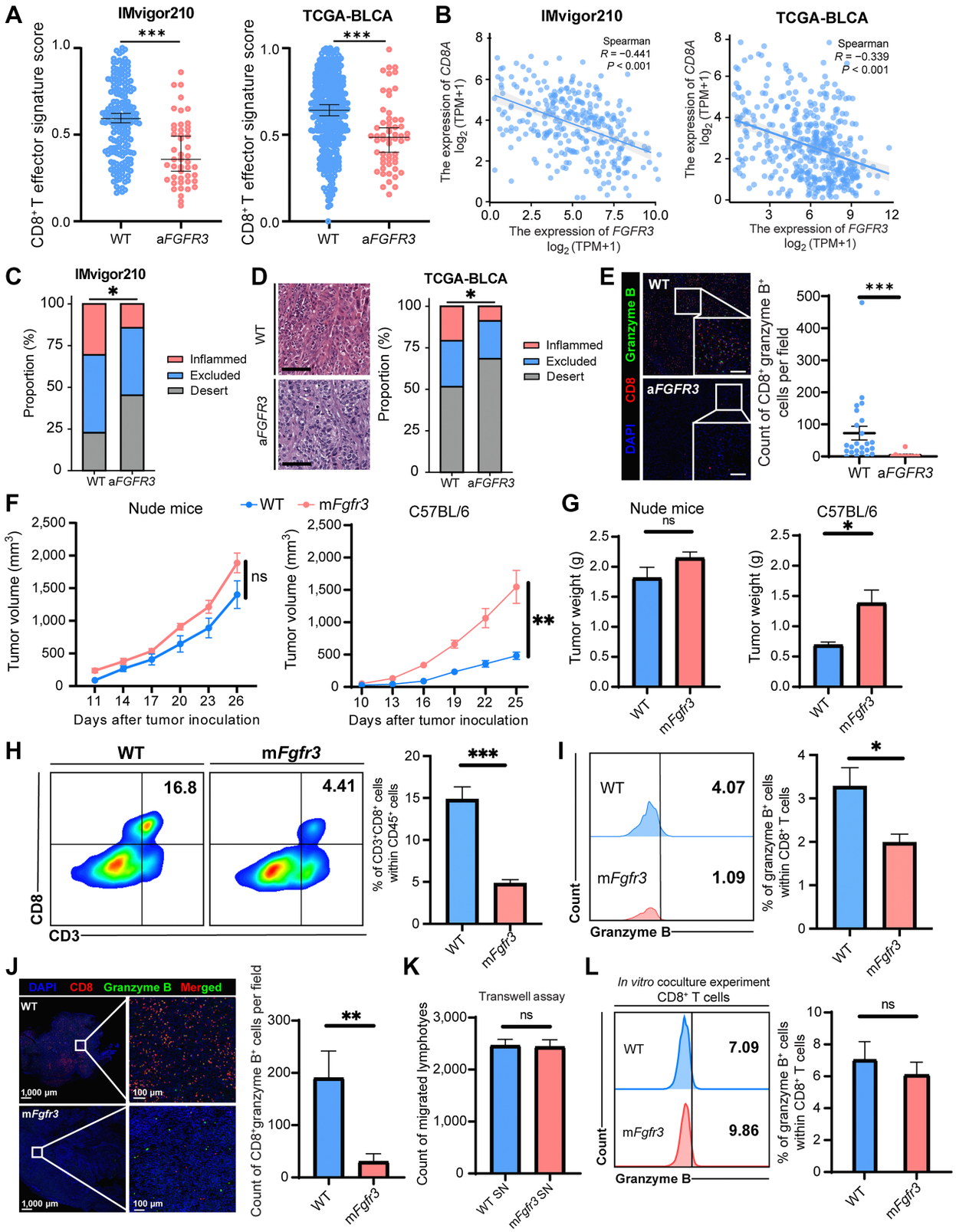
A
IMvigor210
TCGA-BLCA
CD8+ T effector signature score
***
WT
aFGFR3
B
IMvigor210
TCGA-BLCA
Spearman
R = −0.441
P < 0.001
R = −0.339
P < 0.001
The expression of CD8A log2 (TPM+1)
The expression of FGFR3 log2 (TPM+1)
C
IMvigor210
Proportion (%)
Inflammed
Excluded
Desert
D
TCGA-BLCA
E
Granzyme B
CD8
DAPI
Count of CD8+ granzyme B+ cells per field
F
Nude mice
C57BL/6
WT
mFgfr3
Tumor volume (mm3)
ns
**
Days after tumor inoculation
G
Tumor weight (g)
H
16.8
4.41
CD8
CD3
% of CD3+CD8+ cells within CD45+ cells
I
4.07
1.09
Count
Granzyme B
% of granzyme B+ cells within CD8+ T cells
J
DAPI CD8 Granzyme B Merged
1,000 μm
100 μm
Count of CD8+granzyme B+ cells per field
K
Transwell assay
Count of migrated lymphotyes
WT SN
mFgfr3 SN
L
In vitro coculture experiment
CD8+ T cells
7.09
9.86

In addition, we observed a negative correlation between the expression of *CD8A* and *FGFR3* in both datasets (**Fig. 1B**). Tumor-infiltrating lymphocyte phenotypes were investigated, and a lower proportion of inflamed tumor tissues and a higher proportion of immune desert were observed in the a*FGFR3* bladder cancer group in both datasets (**Fig. 1C** and **D**). We also conducted a cohort study at SYSMH to validate this finding. In this cohort, we observed a significant reduction in the infiltration of $CD8^+$ granzyme B^+ cells within the tumors of patients with a*FGFR3* cancers (**Fig. 1E**).

We generated an m*Fgfr3* MB49 cancer cell line to validate our findings in a mouse model. WT and m*Fgfr3* MB49 cells were inoculated into immunodeficient and immunocompetent mice. Surprisingly, there was no difference in tumor growth between WT and m*Fgfr3* cells in immunodeficient mice (**Fig. 1F** and **G**; Supplementary Fig. S1A and S1B). However, m*Fgfr3* tumors exhibited significantly accelerated growth in immunocompetent mice. These results suggested that the enhanced invasiveness of a*FGFR3* cancers was not solely due to intrinsic proliferative changes but may involve immune evasion. We investigated the immune infiltration characteristics of m*Fgfr3* tumors and found a reduction in $CD8^+$ granzyme B^+ T cells through flow cytometry analysis and multiplex IF staining (**Fig. 1H–J**; Supplementary Fig. S1C and S1D).

On the basis of our observations thus far, we hypothesized that a*FGFR3* cancer cells exert their influence on T-cell function and infiltration by excluding T cells from the proximity of cancer cells. We initially speculated that m*Fgfr3* cancer cells might decrease the expression of chemokines, thereby impairing lymphocyte chemotaxis. To test this hypothesis, we conducted a transwell assay, as described in Materials and Methods (Supplementary Fig. S1E). Surprisingly, we did not observe any significant difference in the number of lymphocytes crossing the transwell between the WT and m*Fgfr3* groups (**Fig. 1K**). In addition, we performed a coculture assay by incubating lymphocytes with either WT or m*Fgfr3* cancer cells (Supplementary Fig. S1F). Strikingly, no difference in lymphocyte cytotoxicity was observed between the two groups (**Fig. 1L**). These results collectively suggest that m*Fgfr3* cancer cells cannot modulate lymphocyte migration or directly suppress T-cell functionality.

scRNA-seq highlights the central role of macrophages in inducing the cold TME of the m*Fgfr3* tumor

To investigate the potential involvement of other cell types in mediating immunosuppression within the TME of m*Fgfr3* cancer cells, we conducted scRNA-seq analysis on WT and m*Fgfr3* MB49 tumor tissues. Following quality control and batch effect removal (refer to Materials and Methods: "scRNA-seq of mouse MB49 tumor samples"), we clustered a total of 28,458 single cells into major clusters. Specifically, 14,880 cells were analyzed in the WT group and 13,578 in the m*Fgfr3* group.

We utilized cluster-specific genes and classic markers described in previous studies to annotate the cell types: T cells (*Cd3e*$^+$), $CD8^+$ T cells (*Cd8a*$^+$), $CD4^+$ T conventional cells (*Il7r*$^+$), proliferating T cells (*Hmgb2*$^+$), B cells (*Cd79b*$^+$), myeloid cells (*Lyz2*$^+$), dendritic cells (*Cst3*$^+$), polymorphonuclear leukocytes (*Cxcr2*$^+$), and fibroblasts (*Col1a1*$^+$; **Fig. 2A**; Supplementary Fig. S2A and S2B). Consistent with earlier observations, we identified a significant reduction in the infiltration of $CD8^+$ T cells in the m*Fgfr3* tissues (**Fig. 2B**; Supplementary Fig. S2C).

We next investigated changes in cell-to-cell communication in m*Fgfr3* tumors using the CellChat Package to understand the underlying immune suppression mechanism (26). Specifically, we aimed to identify the key signaling pathway responsible for mediating the immunosuppressive effects on $CD8^+$ T cells. By comparing the incoming pathways between WT and m*Fgfr3* samples, we observed extensive downregulation of the CXCL pathway in the T cells of m*Fgfr3* tissues (Supplementary Fig. S2D). The CXCL signaling pathway is known to play a crucial role in chemotaxis and inflammation, suggesting that reduced CXCL signaling may contribute to the diminished infiltration of cytotoxic lymphocytes and the establishment of an immune-desert TME in m*Fgfr3* tumors. We traced the pathway to further investigate the sources of CXCL signaling and found that macrophages were the main contributors to CXCL signaling in $CD8^+$ T cells in the WT samples (**Fig. 2C**). However, in the m*Fgfr3* tissues, we observed a significant reduction in the CXCL signaling pathway specifically in macrophages. These findings collectively indicate that macrophages play a pivotal role in driving immune suppression in the m*Fgfr3* TME.

We performed a reclustering analysis specifically focusing on macrophages to gain a comprehensive understanding of the characteristics of these cells in m*Fgfr3* tumors, identifying five distinct subclusters (**Fig. 2D**; Supplementary Fig. S2E). Despite the removal of batch effects, macrophages from the two tissue types still showed substantial differences in their expression patterns. Notably, subcluster 1 macrophages were exclusive to m*Fgfr3* tumors. We conducted a differential gene analysis to investigate this distinctive subcluster's molecular characteristics further and found a significant upregulation of *Mrc1*, which encodes CD206 (**Fig. 2E**; Supplementary Fig. S2F). Interestingly, the expression of chemokines (*Cxcl9*, *Cxcl10*, and *Cxcl11*), known for their potent ability to recruit lymphocytes, was notably downregulated in subcluster 1 macrophages. In addition, the expression levels of genes encoding MHC proteins, such as *Cd74*, *H2-Ab1*, and *H2-Eb1*, were also found to be decreased. Gene Ontology (GO) analysis revealed a negative enrichment of pathways associated with antigen processing and presentation and lymphocyte-mediated

Figure 1.

FGFR3-altered bladder cancers shape a cold TME indirectly. **A,** Dot plots showing the $CD8^+$ T cells effector signature score in the WT and a*FGFR3* groups in the IMvigor210 and TCGA-BLCA datasets. **B,** Spearman correlation analysis of the expression of *CD8A* with the expression of *FGFR3*. **C,** Stacked bar plots showing the proportion of immune-inflamed, immune-excluded, and immune-desert phenotypes in the WT and the a*FGFR3* groups in the IMvigor 210 dataset. **D,** Representative images and stacked bar plots indicating the proportion of immune-inflamed, immune-excluded, and immune-desert phenotypes in the WT and the a*FGFR3* groups in TCGA-BLCA dataset. Scale bar, black, 100 μm. **E,** Representative images and dot plot showing the $CD8^+$ granzyme B^+ cells infiltration in the WT and the a*FGFR3* groups in the SYSMH cohort. Scale bar, white, 100 μm. **F** and **G,** Growth curves (**F**) and tumor weights (**G**) of the WT and m*Fgfr3* cancer cells in nude mice as well as C57BL/6 mice. **H** and **I,** Flow cytometry analysis and statistical analysis illustrating the proportion of $CD3^+$ $CD8^+$ cells within $CD45^+$ cells (**H**) and the proportion of granzyme B^+ cells within $CD8^+$ T cells (**I**) in the indicated groups. **J,** Representative images and statistical analysis show the infiltration of $CD8^+$ granzyme B^+ cells in the indicated groups. **K,** Transwell assay of lymphocytes with cancer cell supernatant shows the cell count of migrated lymphocytes in the indicated groups. **L,** Flow cytometry analysis of *in vitro* coculture of cancer cells with lymphocytes illustrating the proportion of granzyme B^+ cells within $CD8^+$ T cells in the indicated groups. The data are shown as the mean ± SEM values (IMVigor 210 cohort: $n = 190$ in the WT group, $n = 47$ in the a*FGFR3* group; TCGA-BLCA cohort: $n = 350$ in the WT group, $n = 56$ in the a*FGFR3* group; SYSMH cohort: $n = 24$ in the WT group, $n = 10$ in the a*FGFR3* group; $n = 6$ per group in **F–L**). $P < 0.05$ was considered a significant difference; ns, no significance (unpaired parametric Student t test and χ^2 test). *, $P < 0.05$; **, $P < 0.01$; ***, $P < 0.001$.

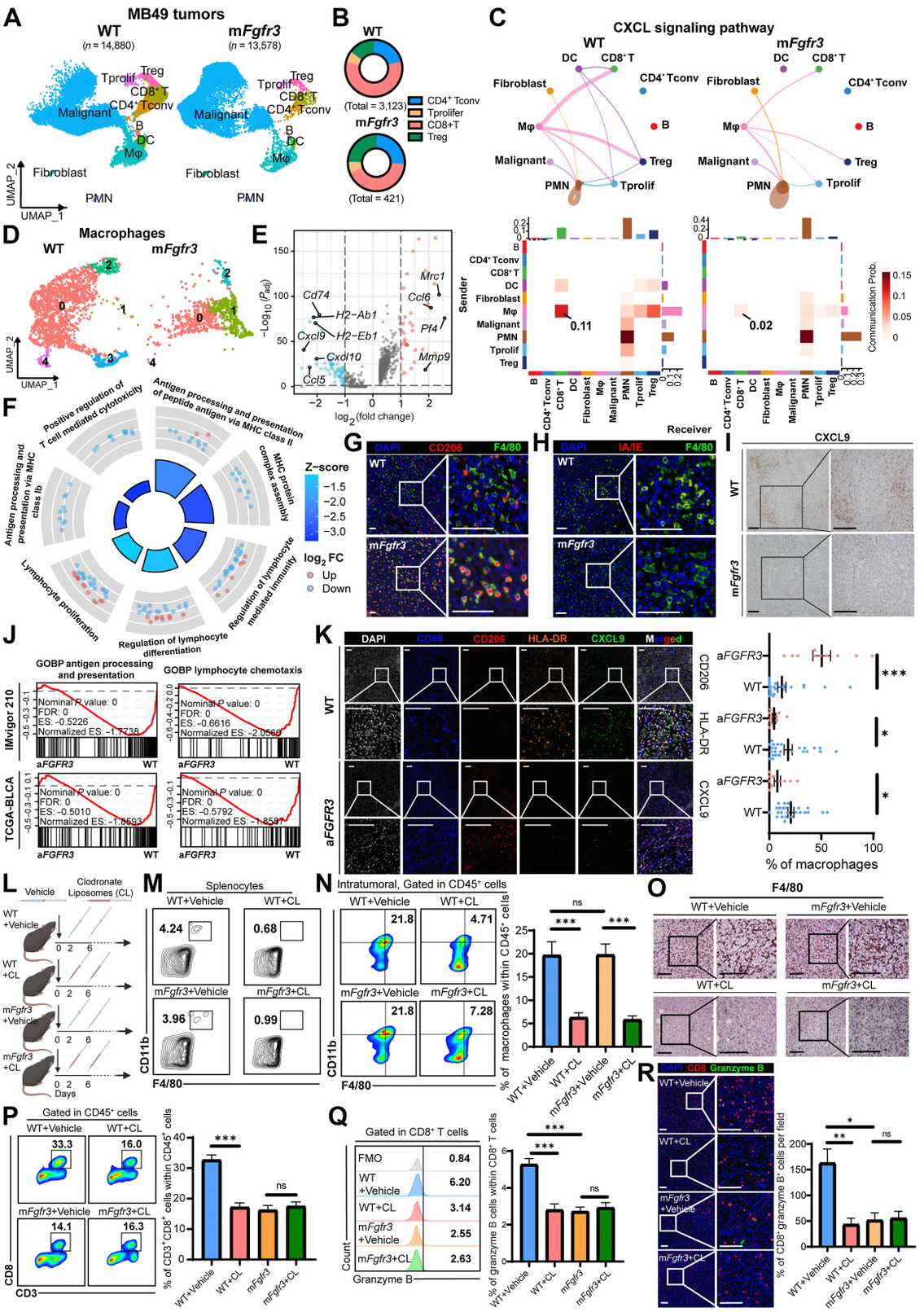
A
MB49 tumors
WT
(n = 14,880)
mFgfr3
(n = 13,578)
Tprolif
Treg
CD8+ T
CD4+ Tconv
Malignant
B
DC
Mφ
Fibroblast
PMN
UMAP_2
UMAP_1
B
WT
(Total = 3,123)
mFgfr3
(Total = 421)
CD4+ Tconv
Tprolifer
CD8+T
Treg
C
CXCL signaling pathway
WT
mFgfr3
DC
CD8+ T
CD4+ Tconv
Fibroblast
Mφ
B
Malignant
Treg
PMN
Tprolif
Sender
Receiver
Communication Prob.
0.11
0.02
D
Macrophages
WT
mFgfr3
E
−Log10 (Padj)
log2 (fold change)
Mrc1
Ccl6
Pf4
Mmp9
Cd74
H2−Ab1
Cxcl9
H2−Eb1
Cxcl10
Ccl5
F
Positive regulation of T cell mediated cytotoxicity
Antigen processing and presentation of peptide antigen via MHC class II
MHC protein complex assembly
Regulation of lymphocyte mediated immunity
Regulation of lymphocyte differentiation
Lymphocyte proliferation
Antigen processing and presentation via MHC class Ib
Z−score
log2 FC
Up
Down
G
DAPI
CD206
F4/80
WT
mFgfr3
H
DAPI
IA/IE
F4/80
I
CXCL9
J
GOBP antigen processing and presentation
GOBP lymphocyte chemotaxis
IMvigor 210
TCGA-BLCA
Nominal P value: 0
FDR: 0
ES: −0.5226
Normalized ES: −1.7738
ES: −0.6616
Normalized ES: −2.0560
ES: −0.5010
Normalized ES: −1.8693
ES: −0.5792
Normalized ES: −1.8587
aFGFR3
WT
K
DAPI
CD68
CD206
HLA-DR
CXCL9
Merged
WT
aFGFR3
aFGFR3
WT
% of macrophages
L
Vehicle
Clodronate Liposomes (CL)
WT +Vehicle
WT +CL
mFgfr3 +Vehicle
mFgfr3 +CL
Days
M
Splenocytes
WT+Vehicle
WT+CL
mFgfr3+Vehicle
mFgfr3+CL
4.24
0.68
3.96
0.99
CD11b
F4/80
N
Intratumoral, Gated in CD45+ cells
21.8
4.71
21.8
7.28
% of macrophages within CD45+ cells
ns
***
O
F4/80
P
Gated in CD45+ cells
33.3
16.0
14.1
16.3
CD8
CD3
% of CD3+CD8+ cells within CD45+ cells
Q
Gated in CD8+ T cells
FMO
0.84
WT +Vehicle
6.20
WT+CL
3.14
mFgfr3 +Vehicle
2.55
mFgfr3+CL
2.63
Count
Granzyme B
% of granzyme B cells within CD8+ T cells
R
DAPI
CD8
Granzyme B
% of CD8+ granzyme B+ cells per field
*
**
ns

immunity in subcluster 1 macrophages (**Fig. 2F**). On the basis of these observations, subcluster 1 macrophages were named "immune-inert macrophages" considering their low expression of lymphocyte-attracting chemokines and a lack of effective T-cell immune response activation through MHC molecule antigen presentation. Collectively, these findings strongly suggest that the capacity of macrophages to process and present antigens and attract lymphocytes is substantially dampened in m*FGFR3* tumor tissues.

We conducted multiplex IF and IHC staining to validate that macrophages adopt an immune-inert phenotype in response to mutant cancer cells. The results obtained were consistent with the scRNA-seq data: we observed an increase in $CD206^+$ macrophages, a decrease in IA/IE^+ macrophages, and reduced expression of CXCL9 in m*Fgfr3* tissues (**Fig. 2G–I**).

We further validated these findings in human bladder cancer cohorts. GSEA of TCGA-BLCA and IMvigor210 datasets revealed a reduction in the pathways related to antigen presenting and processing and lymphocyte chemotaxis in a*FGFR3* tumors (**Fig. 2J**). IHC staining in bladder cancer tumor tissues of the SYSMH cohort confirmed elevated CD206 expression levels in macrophages from a*FGFR3* tumors, while the expression levels of HLA-DR and CXCL9 were reduced (**Fig. 2K**).

We employed a macrophage depletion method using clodronate liposomes to investigate whether macrophages were the driving force behind immune suppression in a*FGFR3* cancers (**Fig. 2L**; Supplementary Fig. S2G–S2I). We aimed to examine immune infiltration in the tissues following macrophage depletion. Both flow cytometry and IHC staining confirmed a significant reduction in macrophage expression in the spleen and tumor tissues (**Fig. 2M–O**; Supplementary Fig. S2J and S2K). In addition, in WT tumors, depleting macrophages led to a significant reduction in $CD8^+$ granzyme B^+ T-cell infiltration, suggesting that macrophages play a vital role in recruiting and activating T cells in the WT TME (**Fig. 2P–R**). In contrast, in the m*Fgfr3* TME, no difference was observed between the control group and the depletion group, validating the limited ability of macrophages in the m*Fgfr3* TME to recruit and activate $CD8^+$ T cells. Taken together, these findings suggest that macrophages play a crucial role in inducing immunosuppression within the TME in tumors with activated *FGFR3*, leading to reduced infiltration of cytotoxic $CD8^+$ T cells.

Next, we collected supernatants from these cancer cells and used them to stimulate BMDMs to investigate whether m*Fgfr3* cancer cells can directly influence macrophage phenotypes (Supplementary Fig. S3A). Flow cytometry and qRT-PCR analysis revealed a significant reduction in the expression of CXCL9 and MHC molecules, accompanied by an increase in CD206 expression in BMDMs stimulated with the mutant group's supernatant (**Fig. 3A–C**; Supplementary Fig. S3B).

We further investigated the functional changes in macrophages with a series of assays. An antigen-presenting assay using OVA was conducted, demonstrating that BMDMs stimulated with m*Fgfr3* supernatants displayed a reduced antigen-presenting ability (**Fig. 3D**). In addition, a transwell assay demonstrated that BMDMs stimulated with m*Fgfr3* supernatant had a significantly diminished capacity to attract lymphocytes compared with those stimulated with WT supernatant (**Fig. 3E**; Supplementary Fig. S3C). Furthermore, an *in vitro* coculture assay with supernatant-stimulated BMDMs and lymphocytes revealed a lower granzyme B level in $CD8^+$ T cells cultured with m*Fgfr3* cell supernatant–treated BMDMs (**Fig. 3F**; Supplementary Fig. S3D).

We extended these experiments by applying supernatants from T24 WT and m*FGFR3* cancer cells to stimulate THP-1 cells. The results were consistent with the data obtained from BMDMs stimulated with MB49 supernatants (**Fig. 3G–I**; Supplementary Fig. S3E).

m*FGFR3* cancer cells upregulate serine synthesis, shifting macrophages to an immune-inert phenotype

We initially hypothesized that bioactive proteins, such as cytokines, might be involved in the mechanism by which m*Fgfr3* cancer cells promote macrophage polarization toward an immune-inert phenotype. To test this hypothesis, we boiled the cancer cell supernatants to denature any bioactive proteins and then used the boiled supernatants to stimulate BMDMs. The purpose was to determine whether the boiling process would abolish the immunosuppressive capacity of the supernatants. Surprisingly, the results showed no discernible difference between the groups treated with boiled and unboiled mutant supernatants. Macrophages stimulated with boiled mutant supernatants displayed an increase in CD206 expression, while the expression levels of MHC molecules and CXCL9 remained reduced (**Fig. 4A–C**). These findings suggested that heat-vulnerable proteins, such as cytokines, were likely not the bioactive factors involved in macrophage polarization. Thus, heat-resistant small-molecule factors are potential contributors.

We conducted a comprehensive analysis of scRNA-seq data to explore the biological characteristics of m*Fgfr3* cancer cells. GSEA revealed a significant upregulation of the pathway involved in amino acid metabolism in the m*Fgfr3* cancer cells compared with WT cells (**Fig. 4D**). Further examination of the differentially expressed genes identified *Psat1* as a significantly upregulated gene in the mutant cells (**Fig. 4E** and **F**). This finding was validated by qRT-PCR, which confirmed the upregulation of *Psat1* in mutant MB49 cells and *PSAT1* in mutant T24 cells (Supplementary Fig. S4A and S4B). IHC staining

Figure 2.

scRNA-seq highlights the central role of macrophages in inducing the cold TME of the m*Fgfr3* tumor. **A,** Uniform Manifold Approximation and Projection (UMAP) plot of scRNA-seq results of WT and m*Fgfr3* MB49 mice tumors colored by major cell types, 14,880 cells in the WT group and 13,578 cells in the m*Fgfr3* group. **B,** Pie chart shows the proportion of subtypes of T lymphocytes in the indicated groups. **C,** Circle plots and heatmap of CellChat analysis show the networks of the CXCL signaling pathway. **D,** UMAP plot of single cells of macrophages colored by subclusters. **E,** Volcano plot displays the differential genes of the subcluster-1 macrophages. **F,** GO analysis represents the enriched pathways in the subcluster-1 macrophages. **G** and **H,** Representative IF images showing the infiltration of $CD206^+$ $F4/80^+$ cells (**G**) and IA/IE^+ $F4/80^+$ cells (**H**) in the indicated groups. **I,** Representative IHC images showing the expression of CXCL9 in the indicated groups. **J,** GSEA showing the enrichment of antigen processing and presenting pathway and lymphocyte chemotaxis pathway in the IMvigor210 and TCGA-BLCA datasets. **K,** Representative multiplex IF images and statistical analysis showing the proportion of $CD206^+$, $HLA\text{-}DR^+$, and $CXCL9^+$ cells within $CD68^+$ macrophages in the SYSMH cohort; $n = 24$ in the WT group, $n = 10$ in the a*FGFR3* group. **L,** Schematic illustration of macrophages depletion strategy with clodronate liposomes in MB49 tumor–bering mice. **M,** Flow cytometry analysis illustrating the proportion of macrophages in the splenocytes in the indicated groups. **N** and **O,** Flow cytometry analysis and IHC staining illustrating the proportion of macrophages in tumors in the indicated groups. **P** and **Q,** Flow cytometry analysis illustrating the proportion of $CD3^+CD8^+$ cells within $CD45^+$ cells (**P**) and the proportion of granzyme B^+ cells within $CD8^+$ T cells (**Q**) in the indicated groups. **R,** Representative IF images and statistical analysis show $CD8^+$ granzyme B^+ cell infiltration in the indicated groups. The data are shown as the mean ± SEM values ($n = 5$ per group). $P < 0.05$ was considered a significant difference; ns, no significance (unpaired parametric Student t test). *, $P < 0.05$; **, $P < 0.01$; ***, $P < 0.001$. Scale bar, 100 μm. FMO, fluorescence minus one; Mφ, macrophages. SN, supernatants. (**L,** Created with BioRender.com.)

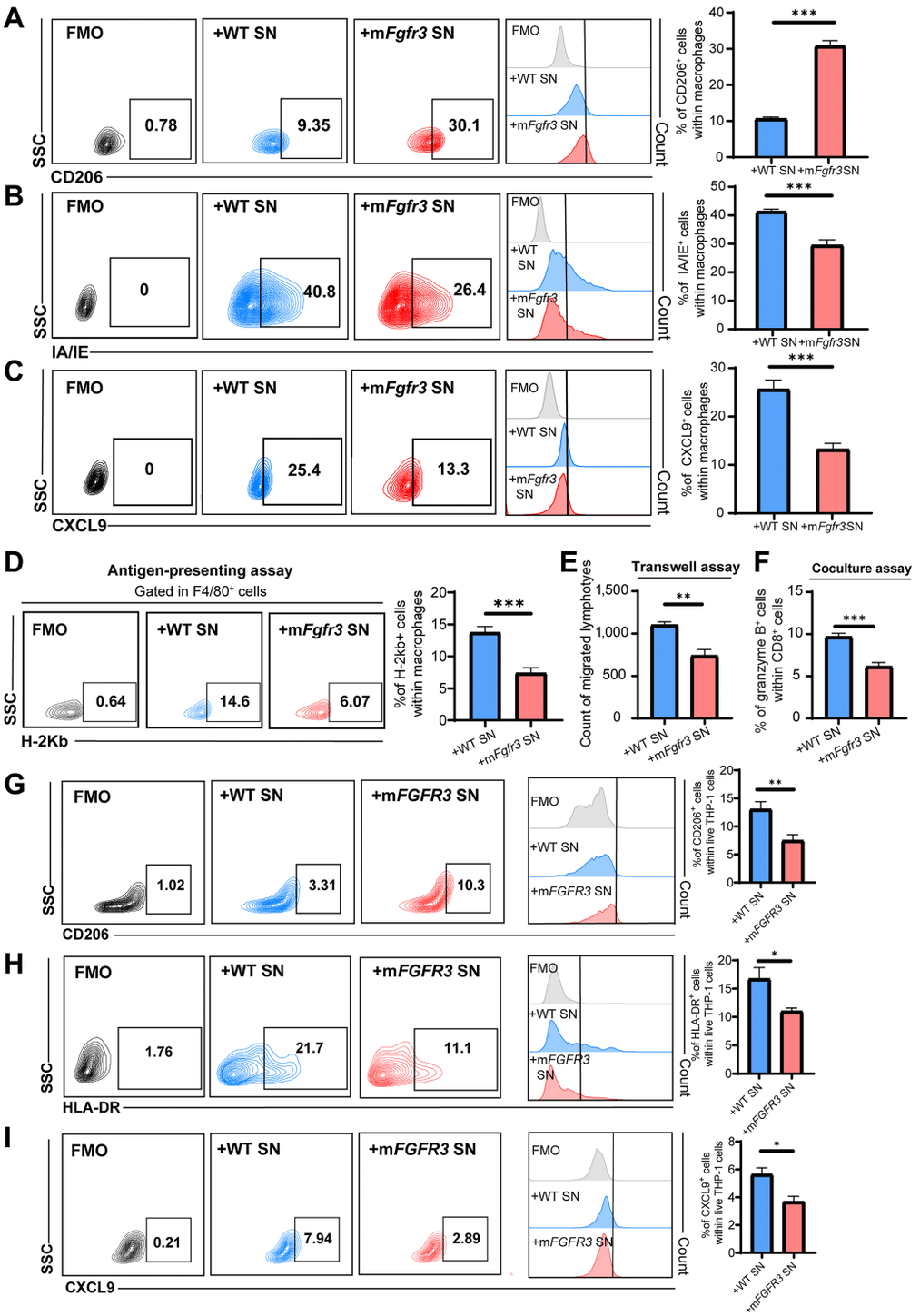

Figure 3.

m*FGFR3* cancer cells promote macrophage shift to an immune-inert phenotype. **A–C,** Flow cytometry analysis and statistical analysis illustrating the proportion of CD206$^+$ cells (**A**), IA/IE$^+$ cells (**B**), and CXCL9$^+$ cells (**C**) within live BMDMs in the indicated groups. **D,** Antigen-presenting assays show the MHC-I SIINFEKL$^+$ cells within the BMDMs. **E,** Transwell assay of lymphocytes with BMDMs previously stimulated by cancer cell supernatants shows the cell count of migrated lymphocytes in the indicated groups. **F,** Flow cytometry analysis of *in vitro* coculture of BMDMs previously stimulated with cancer cell supernatants with lymphocytes illustrating the proportion of granzyme B$^+$ cells within CD8$^+$ T cells in the indicated groups. **G–I,** Flow cytometry analysis and statistical analysis illustrating the proportion of CD206$^+$ cells (**G**), HLA-DR$^+$ cells (**H**), and CXCL9$^+$ cells (**I**) within live THP-1 cells in the indicated groups. The data are shown as the mean ± SEM values ($n = 6$ per group). $P < 0.05$ was considered a significant difference (unpaired parametric Student *t* test). *, $P < 0.05$; **, $P < 0.01$; ***, $P < 0.001$. FMO, fluorescence minus one; SN, supernatants.

was performed to validate these findings in the SYSMH bladder cancer cohort, revealing a significant upregulation of PSAT1 in a*FGFR3* cancers (**Fig. 4G**; Supplementary Fig. S4C). *PSAT1* encodes phosphoserine aminotransferase (PSAT1), an enzyme that plays a role in serine synthesis. Specifically, PSAT1 catalyzes the conversion of phosphohydroxypyruvate (pPYR), derived from glycolysis, to produce phosphoserine (pSER), which is then dephosphorylated to form serine (**Fig. 4H**). Serine quantification assays of cancer cells revealed that the relative serine concentration was elevated in m*FGFR3* cells (**Fig. 4I**). We also examined the serine concentration in BMDMs following stimulation with m*Fgfr3* supernatants. The results showed a significantly higher serine concentration than that in BMDMs supplemented with WT supernatant (**Fig. 4J**). We supplemented the WT supernatant with serine for BMDM stimulation to further explore the role of serine in macrophage phenotype shifting. Flow cytometry analysis revealed that adding serine to the WT supernatant had similar effects to supernatant from mutant cells. Macrophages stimulated with serine-supplemented WT supernatant demonstrated increased expression of CD206 and reduced expression of CXCL9 and IA/IE (**Fig. 4K–M**). Consistent results were obtained when THP-1 cells were stimulated with serine-supplemented T24 WT supernatant (Supplementary **Fig. 4D–F**). Antigen-presenting assays and a transwell assay of serine-supplemented BMDMs were also performed, and their results also confirmed that adding serine to the WT supernatant showed effects comparable with those of the mutant cell supernatant (**Fig. 4N** and **O**).

Next, we aimed to investigate the functional consequences of blocking the serine influx in BMDMs using L-phenylglycine, a recognized inhibitor of serine transporters. A serine assay confirmed that the serine concentration in BMDMs stimulated with m*Fgfr3* supernatants and treated with L-phenylglycine was reduced and comparable with that of the WT group (**Fig. 4P**). Flow cytometry analysis was subsequently conducted, revealing that after blocking serine influx in BMDMs, the macrophage phenotype in the m*Fgfr3* group became similar to that of the WT group (**Fig. 4Q–S**). Based on these results, we can conclude that serine controls the macrophage phenotype in the m*Fgfr3* TME.

Because the MAPK pathway is regarded as the predominant downstream signaling pathway of FGFR, we hypothesized that activating FGFR3 might upregulate PSAT1 expression through MAPK signaling (**Fig. 4T**; ref. 27). Two ERK isoforms, ERK1/2 and ERK5, have been previously reported. In our study, increases in both pERK1/2 and pERK5 expression in mutant cancer cells were observed by Western blotting. Inhibition of ERK1/2 rather than ERK5 reduced the expression of PSAT1 in MB49 cancer cells, but in the T24 cells, inhibition of either ERK1/2 or ERK5 could prevent the upregulation of PSAT1 (Supplementary Fig. S4G).

Targeting the PI3K/Akt pathway in macrophages reverses macrophage phenotypes in m*FGFR3* cancers

We investigated the underlying signaling pathway responsible for the induced phenotype shift to determine how to reverse the macrophage phenotype shifts in m*Fgfr3* cancers. Considering the various pathways associated with macrophage phenotype modulation, we performed GSEA on well-established signaling pathways (Supplementary Table S2; ref. 28). The analysis revealed the PI3K/Akt signaling pathway, known to play a crucial role in macrophage phenotype conversion, to be the most enriched pathway (**Fig. 5A**). This pathway is known to regulate the expression of CD206, CXCL9, and MHC in macrophages (29–32). We assessed the phosphorylation levels of Akt in macrophages upon stimulation with m*Fgfr3* or WT cell supernatant to validate the involvement of the PI3K/Akt pathway in m*Fgfr3* supernatant–induced macrophage polarization. Significantly elevated Akt phosphorylation was observed in BMDMs exposed to m*Fgfr3* cell supernatant compared with that in those stimulated with WT cell supernatant (**Fig. 5B**; Supplementary Fig. S5A). Furthermore, supplementation of serine in BMDMs cultured with WT cancer supernatant increased Akt phosphorylation (**Fig. 5C**; Supplementary Fig. S5B).

The mechanism by which serine activates the PI3K/Akt pathway in macrophages remains unclear. Serine is primarily involved in providing methyl donors for DNA and protein methylation. Thus, we hypothesized that elevated serine levels in m*Fgfr3* cancer cells promote PI3K/Akt pathway activation by enhancing intracellular methylation. Therefore, we supplemented the WT cell supernatant with SAM, a universal methyl donor. The results showed that SAM supplementation resulted in similar changes in Akt phosphorylation as those observed with elevated serine levels (**Fig. 5D**; Supplementary Fig. S5C). This finding suggests that exogenous serine may enhance intracellular methylation activities, thereby activating macrophage Akt.

Duvelisib is a potent inhibitor of PI3Kδ and PI3Kγ, constitutively expressed in leukocytes, and is FDA approved for certain hematologic malignancies (33). We treated BMDMs stimulated with cancer cell supernatant with duvelisib to investigate whether targeting the PI3K/Akt pathway could reverse the immunosuppressive effects of m*Fgfr3* cancer cell supernatant. Flow cytometry analysis showed that duvelisib successfully abolished the elevation of Akt expression in macrophages cultured with m*Fgfr3* supernatant (**Fig. 5E**; Supplementary Fig. S5D). Furthermore, duvelisib reduced the expression of CD206 and restored the expression of CXCL9 and MHC molecules in macrophages treated with m*Fgfr3* supernatant (**Fig. 5F–H**; Supplementary Fig. S5E–S5G). Meanwhile, cell viability assays indicated that duvelisib had no inhibitory effect on cancer cell proliferation (Supplementary Fig. S5H and S5I). We subsequently investigated the *in vivo* antitumor efficacy of duvelisib in C57BL/6 mice bearing WT or m*Fgfr3* MB49 tumors (Supplementary Fig. S5J). Consistent with previous findings, m*Fgfr3* tumors exhibited accelerated growth compared with that of WT tumors. However, duvelisib treatment effectively inhibited the growth of m*Fgfr3* tumors, resulting in reduced tumor weights (**Fig. 5I** and **J**; Supplementary Fig. S5K). In contrast, WT tumors did not show significant responsiveness to duvelisib treatment, with no considerable differences in tumor growth and weight between the treatment and control groups. Multiplex IF analysis confirmed the reduction in $CD206^+$ macrophages within m*Fgfr3* tumor tissues following duvelisib treatment (**Fig. 5K**; Supplementary Fig. S5L). Flow cytometry analysis revealed decreased production of CXCL9 and expression of IA/IE by macrophages in the m*Fgfr3* group compared with that in the WT group (**Fig. 5L** and **M**; Supplementary Fig. S5M–S5O). Duvelisib treatment reversed the effects of m*Fgfr3* cancer cells and enhanced the secretion of CXCL9 and expression of IA/IE by macrophages. In addition, an increased frequency of $CD8^+$ granzyme B^+ T cells was detected in m*Fgfr3* tumors treated with duvelisib (**Fig. 5N–P**; Supplementary Fig. S5P–S5S).

The above results demonstrated that duvelisib significantly impacts mouse m*Fgfr3* MB49 tumors. Hence, we applied it in humanized mice bearing m*FGFR3* T24 tumors (**Fig. 5Q**). The results demonstrated that duvelisib could also significantly delay the growth of m*FGFR3* T24 tumors, and we noticed a reduction in tumor weights in this treatment group (**Fig. 5R–T**). Immune infiltration in the tumors was consistent with the above data: reduced $CD206^+$ cells and increased $CD8^+$ T cells

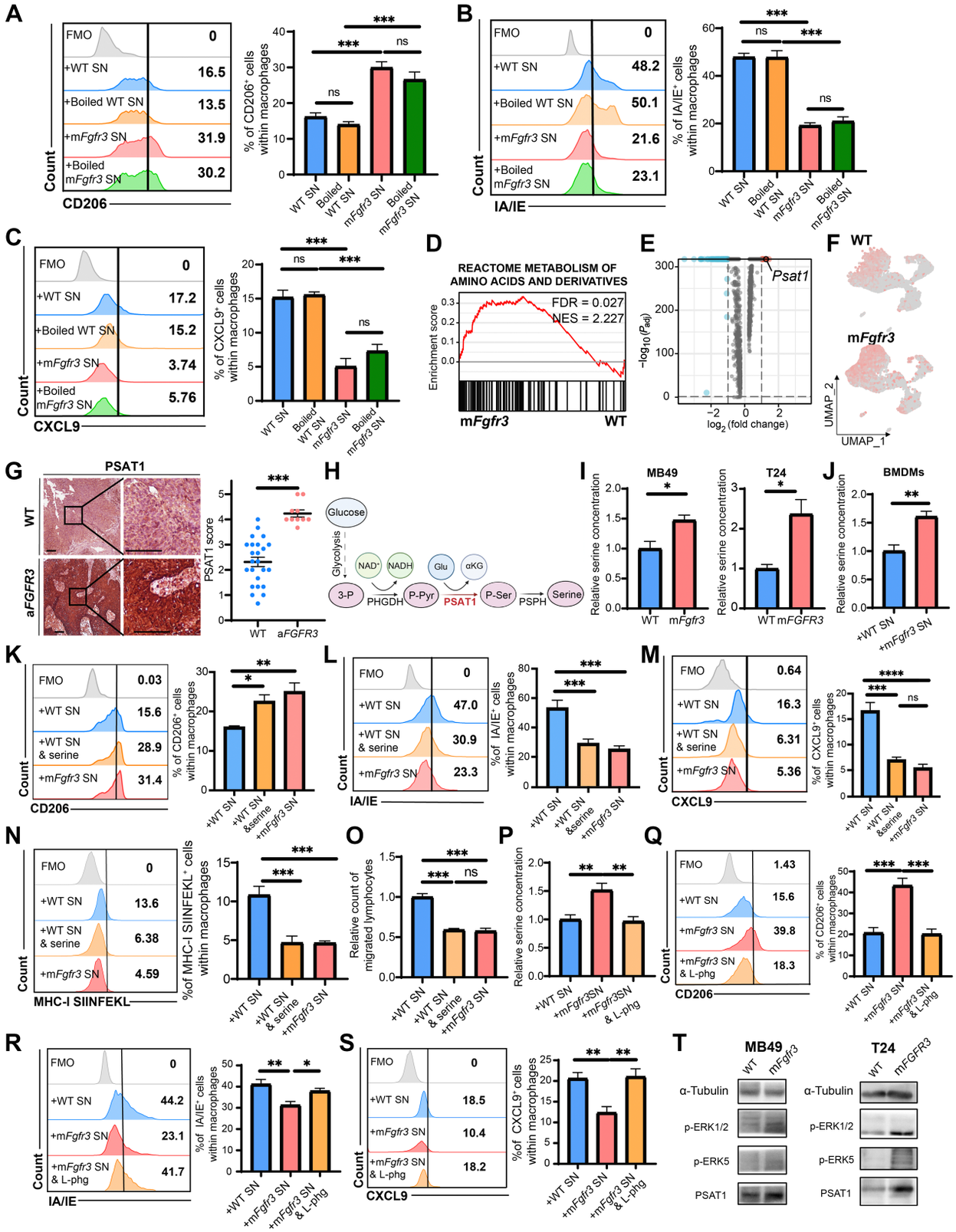
A
FMO
+WT SN
+Boiled WT SN
+mFgfr3 SN
+Boiled mFgfr3 SN
0
16.5
13.5
31.9
30.2
Count
CD206
% of CD206+ cells within macrophages
WT SN
Boiled WT SN
mFgfr3 SN
Boiled mFgfr3 SN
B
48.2
50.1
21.6
23.1
IA/IE
% of IA/IE+ cells within macrophages
C
17.2
15.2
3.74
5.76
CXCL9
% of CXCL9+ cells within macrophages
D
REACTOME METABOLISM OF AMINO ACIDS AND DERIVATIVES
FDR = 0.027
NES = 2.227
Enrichment score
mFgfr3
WT
E
Psat1
−log10 (Padj)
log2 (fold change)
F
WT
mFgfr3
UMAP_2
UMAP_1
G
PSAT1
WT
aFGFR3
PSAT1 score
H
Glucose
Glycolysis
NAD+
NADH
Glu
αKG
3-P
PHGDH
P-Pyr
PSAT1
P-Ser
PSPH
Serine
I
MB49
T24
Relative serine concentration
WT
mFgfr3
mFGFR3
J
BMDMs
+WT SN
+mFgfr3 SN
K
0.03
15.6
28.9
31.4
+WT SN & serine
&serine
L
47.0
30.9
23.3
M
0.64
16.3
6.31
5.36
N
13.6
6.38
4.59
MHC-I SIINFEKL
%of MHC-I SIINFEKL+ cells within macrophages
O
Relative count of migrated lymphocytes
P
Relative serine concentration
+mFgfr3SN
Q
1.43
15.6
39.8
18.3
+mFgfr3 SN & L-phg
R
44.2
23.1
41.7
S
18.5
10.4
18.2
T
MB49
T24
α-Tubulin
p-ERK1/2
p-ERK5
PSAT1

were seen in the duvelisib treatment group (**Fig. 5U** and **V**; Supplementary Fig. S5T and S5U).

Duvelisib augments the antitumor efficacy of erdafitinib in combination therapy

Duvelisib effectively reprogrammed the TME of mutant tumors by restoring the immune-inert macrophages back to an active phenotype. Subsequently, we assessed the antitumor efficacy of duvelisib in combination with erdafitinib in m*Fgfr3* tumor-bearing C57BL/6 mice (**Fig. 6A**). *In vitro* cell viability assays indicated that erdafitinib has an inhibiting effect on cancer cell growth (Supplementary Fig. S6A). Compared with the vehicle treatment, duvelisib, and erdafitinib monotherapy significantly delayed tumor growth (**Fig. 6B–D**). Notably, compared with monotherapy, the combination of duvelisib and erdafitinib demonstrated enhanced suppression of tumor growth and reduced tumor weight. Multiplex IF analysis revealed a marked reduction in the number of $CD206^+$ cells in the monotherapy groups, with even lower infiltration observed in the combination treatment group (**Fig. 6E**). Flow cytometry analysis demonstrated that both duvelisib and erdafitinib upregulated the expression of CXCL9 and IA/IE by macrophages (**Fig. 6F** and **G**). Consequently, $CD8^+$ granzyme B^+ T-cell infiltration increased (**Fig. 6H–J**). Importantly, the combination of erdafitinib with duvelisib further improved CXCL9 secretion, IA/IE expression, and $CD8^+$ T-cell infiltration.

We also investigated the efficacy of these combination therapies in nude mice with m*Fgfr3* MB49 tumors. Our findings demonstrated that treatment with erdafitinib as a monotherapy partially delayed tumor growth (Supplementary Fig. S6B–S6D). However, duvelisib showed no efficacy in immune-deficient mice when administered as a monotherapy. This observation further reinforces the notion that duvelisib can effectively slow tumor growth by modulating immune responses specifically in immune-competent mice. Notably, the combination therapy exhibited comparable results to erdafitinib monotherapy.

Discussion

This study provided evidence of a*FGFR3* tumors being correlated with an immune-desert TME characterized by low numbers of inactive $CD8^+$ T cells. We found that heightened serine synthesis in m*FGFR3* cancer cells induces an immunologically cold state by shifting macrophages toward the immune-inert subtype, marked by impaired antigen presentation and T-cell chemotaxis. Moreover, we uncovered the mechanism through which increased serine efflux from mutant cancer cells activates Akt kinase activity, leading to the upregulation of CD206 expression and the downregulation of MHC molecules and CXCL9 expression in macrophages. We devised a novel therapeutic strategy using a PI3K inhibitor to inhibit macrophage reprogramming and enhance the treatment efficacy of erdafitinib in m*Fgfr3* bladder cancers.

Several studies have indicated the association of a*FGFR3* tumors with an immune-desert TME. For example, it has been shown that a*FGFR3* tumors are more prevalent in the luminal or luminal papillary subtypes, which are typically characterized by fewer T-cell inflammatory responses (9). In addition, according to the results of the BLC2001 study of erdafitinib, only 5% of a*FGFR3* patients respond to prior ICIs treatment, suggesting that a*FGFR3* cancers are associated with a more deleterious TME refractory to ICIs treatment (7). A similar trend was observed in a study of rogaratinib, which included 10 patients, with 90% displaying unresponsiveness to previous immunotherapy (34). Some people suggested that the PD-1/PD-L1 axis could be activated through *FGFR* activation in cancer cells (12, 13, 35). Nevertheless, this explanation does not account for the observed scarcity of cytotoxic T-cell infiltration or the limited response rate to ICIs treatment in these patients. In the current study, we demonstrate that cancer cells with *FGFR3* alterations do not directly influence T-cell chemotaxis or functionality. Conversely, it was revealed that these cancer cells hijacked macrophages, inducing their phenotypic shift toward an immune-inert state, thus playing a pivotal role in establishing the immunosuppressive microenvironment.

Metabolic alterations have often been observed in cancer cells with oncogenic activation, which was previously considered a cell-autonomous adaptation (36). Recent findings have suggested that oncogene activation plays a causative rather than a correlative role in reprogramming metabolic phenotypes in malignant cells (37). For example, in a recent study by Nan, activation of oncogenic tyrosine kinase receptors, such as *FGFR* activation in non–small cell lung carcinoma, enhanced aerobic glycolysis and recycled lactate (16). In melanoma, oncogenic BRAF activates the MAPK pathway, upregulates aerobic glycolysis, and enhances reliance on glutamine utilization (38). In this study, our results showed that *FGFR3* activation in bladder cancer cells could upregulate PSAT1 expression and branch glycolysis to serine synthesis through the MAPK pathway. Serine is the fundamental building block essential for sustaining life. In addition to its role in protein synthesis, serine is involved in various metabolic pathways, including redox balance, nucleotide synthesis, and one-carbon metabolism (19, 39). One-carbon metabolism consists of the folate and methionine cycle and integrates carbon units from serine, generating various products, including substrates for methylation reactions (40). Intracellular nucleotide and protein methylation influence transcription, translation, and posttranslational protein function and stability. Cancer cells utilize these pathways to support uncontrolled

Figure 4.

m*FGFR3* cancer cells upregulate serine synthesis to shift macrophages to an immune-inert phenotype. **A–C,** Flow cytometry analysis illustrating the proportion of $CD206^+$ cells (**A**), IA/IE^+ cells (**B**), and $CXCL9^+$ cells (**C**) within BMDMs stimulated with unboiled/ boiled WT/ m*Fgfr3* cancer cells supernatants. **D,** GSEA showing the metabolism of amino acid and derivatives pathway is enriched in the m*Fgfr3* cancer cells. **E,** Volcano plot displays the marker genes of the m*Fgfr3* cancer cells. **F,** FeaturePlot shows the expression of *Psat1* in the WT and m*Fgfr3* cancer cells. **G,** Representative IHC pictures and statistic analysis show the expression of PSAT1 in the WT and a*FGFR3* tumors; $n = 24$ in the WT group, $n = 10$ in the a*FGFR3* group. **H,** Schematic illustration of the role of PSAT1 in the serine synthesis metabolism. **I,** Relative free serine concentration of the WT and m*Fgfr3* MB49 cells or WT and m*FGFR3* T24 cancer cells. **J,** Relative free serine concentration of the BMDMs stimulated with WT and m*Fgfr3* cancer cell supernatants. **K–M,** Flow cytometry analysis and statistical analysis illustrating the proportion of $CD206^+$ cells (**K**), IA/IE^+ cells (**L**), and $CXCL9^+$ cells (**M**) within BMDMs in the indicated groups. **N,** Antigen-presenting assay shows the MHC-I $SIINFEKL^+$ cells within the BMDMs. **O,** Transwell assay of lymphocytes with BMDMs previously stimulated by cancer cell supernatants shows the cell count of migrated lymphocytes in the indicated groups. **P,** Relative free serine concentration of the BMDMs in the indicated groups. **Q–S,** Flow cytometry analysis and statistical analysis illustrating the proportion of $CD206^+$ cells (**Q**), IA/IE^+ cells (**R**), and $CXCL9^+$ cells (**S**) within BMDMs in the indicated groups. **T,** Western blot analysis indicates the phosphorylation level of the MAPK pathway as well as the PSAT1 expression in the indicated groups. The data are shown as the mean ± SEM values ($n = 6$ per group in **A–C, N–O**, and **Q–S**; $n = 4$ per group in **I**; $n = 5$ per group in **J–M** and **P**) or are representative of three independent experiments (**T**). $P < 0.05$ was considered a significant difference; ns, no significance (one-way ANOVA with Holm-Sidak multiple comparison tests, unpaired parametric Student *t* test). *, $P < 0.05$; **, $P < 0.01$; ***, $P < 0.001$. Scale bar, white, 100 μm. FMO, fluorescence minus one; SN, supernatants. (**H,** Created with BioRender.com.)

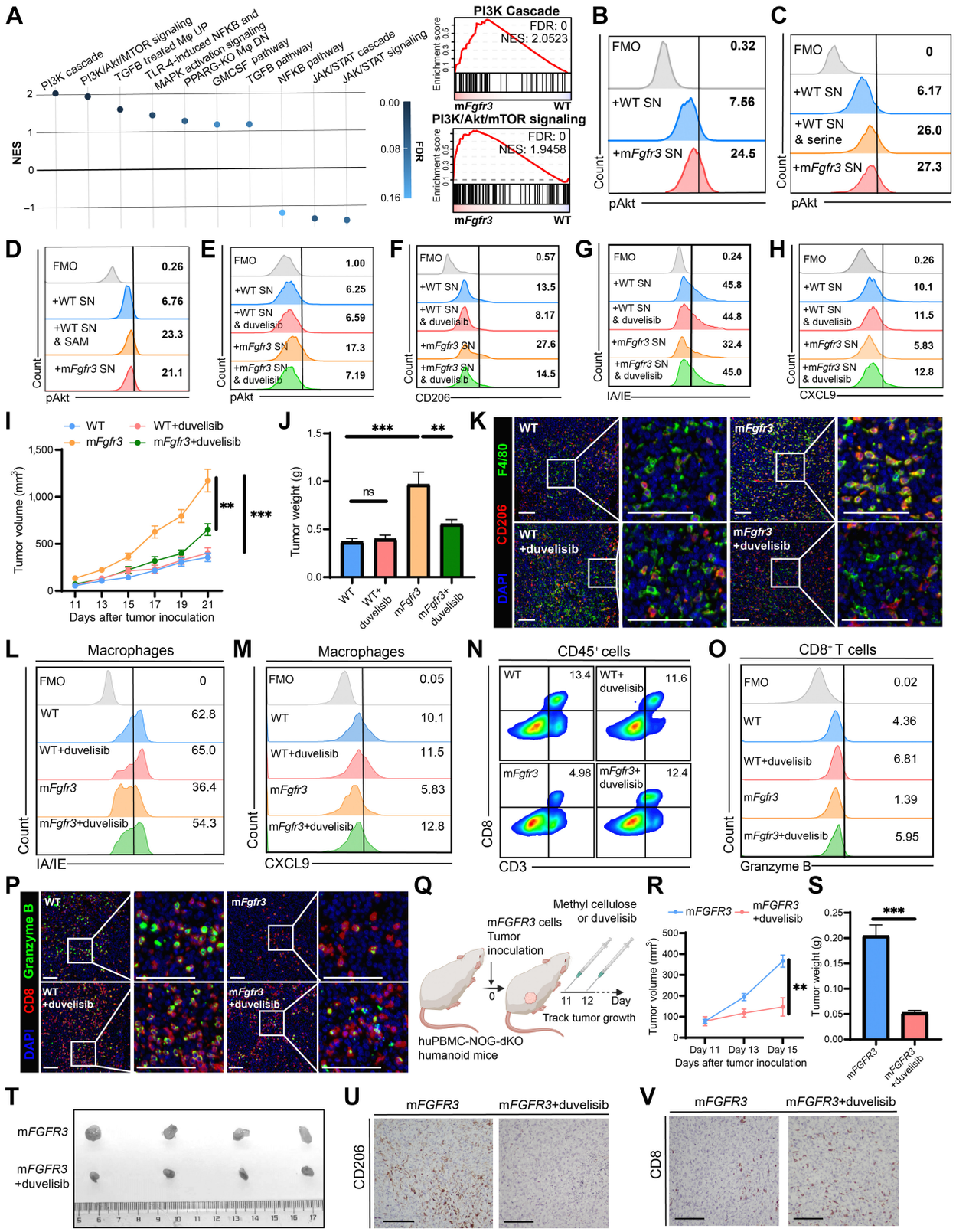
A
PI3K cascade
PI3K/Akt/MTOR signaling
TGFB treated Mφ UP
TLR-4-induced NFKB and MAPK activation signaling
PPARG-KO Mφ DN
GMCSF pathway
TGFB pathway
NFKB pathway
JAK/STAT cascade
JAK/STAT signaling
NES
FDR
PI3K Cascade
FDR: 0
NES: 2.0523
PI3K/Akt/mTOR signaling
FDR: 0
NES: 1.9458
Enrichment score
mFgfr3
WT
B
FMO 0.32
+WT SN 7.56
+mFgfr3 SN 24.5
Count
pAkt
C
FMO 0
+WT SN 6.17
+WT SN & serine 26.0
+mFgfr3 SN 27.3
D
FMO 0.26
+WT SN 6.76
+WT SN & SAM 23.3
+mFgfr3 SN 21.1
E
FMO 1.00
+WT SN 6.25
+WT SN & duvelisib 6.59
+mFgfr3 SN 17.3
+mFgfr3 SN & duvelisib 7.19
F
FMO 0.57
+WT SN 13.5
+WT SN & duvelisib 8.17
+mFgfr3 SN 27.6
+mFgfr3 SN & duvelisib 14.5
CD206
G
FMO 0.24
+WT SN 45.8
+WT SN & duvelisib 44.8
+mFgfr3 SN 32.4
+mFgfr3 SN & duvelisib 45.0
IA/IE
H
FMO 0.26
+WT SN 10.1
+WT SN & duvelisib 11.5
+mFgfr3 SN 5.83
+mFgfr3 SN & duvelisib 12.8
CXCL9
I
WT
WT+duvelisib
mFgfr3
mFgfr3+duvelisib
Tumor volume (mm3)
Days after tumor inoculation
J
Tumor weight (g)
ns
K
F4/80
CD206
DAPI
WT
WT +duvelisib
mFgfr3
mFgfr3 +duvelisib
L
Macrophages
FMO 0
WT 62.8
WT+duvelisib 65.0
mFgfr3 36.4
mFgfr3+duvelisib 54.3
M
Macrophages
FMO 0.05
WT 10.1
WT+duvelisib 11.5
mFgfr3 5.83
mFgfr3+duvelisib 12.8
N
CD45+ cells
WT 13.4
WT+ duvelisib 11.6
mFgfr3 4.98
mFgfr3+ duvelisib 12.4
CD8
CD3
O
CD8+ T cells
FMO 0.02
WT 4.36
WT+duvelisib 6.81
mFgfr3 1.39
mFgfr3+duvelisib 5.95
Granzyme B
P
Granzyme B
CD8
DAPI
WT
WT +duvelisib
mFgfr3
mFgfr3 +duvelisib
Q
mFGFR3 cells
Tumor inoculation
Methyl cellulose or duvelisib
Track tumor growth
huPBMC-NOG-dKO humanoid mice
R
mFGFR3
mFGFR3 +duvelisib
Tumor volume (mm3)
Day 11 Day 13 Day 15
Days after tumor inoculation
S
Tumor weight (g)
mFGFR3
mFGFR3 +duvelisib
T
mFGFR3
mFGFR3 +duvelisib
U
mFGFR3
mFGFR3+duvelisib
CD206
V
mFGFR3
mFGFR3+duvelisib
CD8

proliferation and survival, with enhanced aerobic glycolysis resulting in serine overproduction.

The implications of serine metabolism in the TME extend beyond cancer cell proliferation. Serine metabolism also influences the functionality and phenotypes of immune cells. Previous studies have demonstrated that the metabolic status of immune cells is critical due to their dynamic activation states (20, 41). For example, Ma and colleagues (42) revealed that serine metabolism is required for effector T-cell expansion by fueling nucleotide biosynthesis and one-carbon metabolism. However, in the TME, most immune cells proliferate at a relatively slow rate, and serine synthesis in these cells is less active. In contrast, highly proliferating cancer cells that hyperactivate serine synthesis are the major source of serine in the TME (43). We believe this discrepancy in serine metabolism between cancer cells and immune cells has profound implications for immune cell function. In this study, our findings strongly suggest that the overproduction of serine from cancer cells, specifically m*FGFR3* cells, plays a crucial role in macrophage phenotypic shifts toward an immune-inert state. This effect is evidenced by the downregulation of MHC molecules and the CXCL9 chemokines. The observed immune-inert phenotype in macrophages within the TME could potentially impair their ability to mount an effective immune response against cancer cells.

Some previous studies have suggested that in noncancer settings, macrophages are influenced by intracellular serine metabolism alteration. For example, a recent study demonstrated that serine metabolism deficiency in macrophages activated the p38-dependent JAK-STAT1 axis (44). In another study, intracellular serine metabolism was found to activate mTOR signaling and support IL1β production in macrophages (45). However, the precise mechanism by which macrophages are influenced by serine efflux remains controversial. In this study, we aimed to investigate the signaling pathways that regulate macrophage phenotype switching in response to serine efflux. Our screening process identified the PI3K/Akt pathway as the most upregulated pathway in macrophages from the m*Fgfr3* group. Subsequent experiments confirmed that serine supplementation increased Akt phosphorylation levels and induced substantial phenotype changes in macrophages. These findings provide novel insights into the mechanisms underlying the influence of serine efflux on macrophages. The upregulation of the PI3K/Akt pathway and its subsequent effects on macrophage phenotypes suggest a potential molecular mechanism involved in the serine-mediated modulation of immune responses.

The PI3K/Akt signaling has been best studied in tumorigenesis, where activating *PI3K* mutations or inactivating *PTEN* mutations represent frequent mutations in various cancer types (46). It is known that the PI3K/Akt pathway plays a vital role in macrophage phenotype modulation. For instance, Kaneda and colleagues indicated that PI3K inhibition enhanced the expression of MHC II and proinflammatory cytokines and inhibited the expression of immune suppressive factors in macrophages, indicating that PI3K controls the switch between immune suppression and immune stimulation (30). Other studies have validated this finding (31, 32). However, how this pathway is regulated in the macrophages remains largely unclear. According to studies on the PI3K/Akt signaling in cancer cells, in addition to the classic Akt-activating steps, several posttranslational modifications fine-tune Akt activity, including methylation, phosphorylation, and ubiquitination (47–49). Here, our studies showed that exogenous serine or SAM supplementation could enhance the phosphorylation level of Akt in macrophages, suggesting that enhancing intracellular methylation activities in macrophages promotes Akt activity. Several previous studies have demonstrated that increased Akt protein methylation promotes phosphorylation and enhances kinase activities (50, 51), which might be the trigger point of serine-induced Akt activation in macrophages.

PI3Ks consist of a regulatory subunit with a p110 catalytic subunit (p110α, β, γ, or δ; ref. 52). Herein, these heterodimeric complexes are referred to as PI3Kα, PI3Kβ, PI3Kγ, and PI3Kδ, with p110α, p110β, p110γ, and p110δ indicating the catalytic subunits themselves. p110α and p110β showed broad tissue distribution, whereas p110γ and p110δ were highly enriched in all leukocyte subtypes. Traditionally, the clinical application of pan-PI3K inhibitors in cancer settings has been limited because of their adverse cardiovascular and metabolic adverse effects (53). Several studies have indicated that compared with the pan-PI3K inhibitors, selective PI3K inhibitors in leukocytes have a better safety profile (54). Duvelisib, a selective PI3Kδ and PI3Kγ inhibitor, has been approved for the treatment of several types of lymphoma (33). In this study, we demonstrated that the selective inhibition of PI3K exhibits significant antitumor efficacy in a*FGFR3* cancers due to the considerable upregulation of the PI3K/Akt pathway in macrophages.

Conclusion

In this study, we revealed that a*FGFR3* cancers are associated with a non–T-cell–inflamed TME. We subsequently found that by activating the PI3K/Akt pathway, increased serine synthesis from m*FGFR3* cancer cells shifted macrophages to an immune-inert phenotype characterized by reduced expressed chemokines for lymphocytes chemotaxis and MHC molecules, resulting in the promotion of a cold immune TME. We further suggest that redirecting the macrophage phenotype with PI3K inhibitors has the potential to enhance the antitumor efficacy of erdafitinib in a*FGFR3* tumors.

Figure 5.

Targeting the PI3K/Akt pathway in macrophages reverses macrophage phenotype in m*FGFR3* cancers. **A,** Bubble chart of GSEA results involving the major pathways regulating macrophage phenotype in the macrophages cells from m*Fgfr3* cancers compared with the ones from WT cancers, along with enrichment results of the PI3K cascade pathway as well as PI3K/Akt/mTOR signaling pathway, Mφ, macrophages. **B–D,** Flow cytometry analysis illustrating the proportion of $pAKT^+$ cells within BMDMs in the indicated groups. **E–H,** Flow cytometry analysis illustrating the proportion of $pAKT^+$ cells (**E**), $CD206^+$ cells (**F**), IA/IE^+ cells (**G**), and $CXCL9^+$ cells (**H**) within BMDMs in the indicated groups. **I** and **J,** Tumor growth curves (**I**) and tumor weights (**J**) of the indicated groups in the duvelisib monotherapy experiments. **K,** Representative images show the infiltration of $CD206^+$ $F4/80^+$ cells in the indicated groups. **L** and **M,** Flow cytometry analysis illustrating the proportion of IA/IE^+ cells (**L**) and $CXCL9^+$ cells (**M**) within macrophages in the indicated groups. **N** and **O,** Flow cytometry analysis illustrating the proportion of $CD3^+CD8^+$ cells within $CD45^+$ cells (**N**) and the proportion of granzyme B^+ cells within $CD8^+$ T cells (**O**) in the indicated groups. **P,** Representative images show $CD8^+$ granzyme B^+ cell infiltration in the indicated groups. **Q,** Schematic illustration of duvelisib treatment strategy in huPBMC-NOG-dKO humanoid mice bearing m*FGFR3* T24 tumors. **R–T,** Tumor growth curves (**R**), tumor weights (**S**), and the resected tumor picture (**T**) of the indicated groups in the duvelisib treatment experiment on the humanoid mice. **U** and **V,** IHC staining indicates the CD206 (**U**) and CD8 (**V**) infiltration in the indicated groups from the humanoid mice experiment. The data are shown as the mean ± SEM values ($n = 6$ per group in **B, C,** and **E–J**; $n = 4$ per group in **R** and **S**; $n = 3$ per group in **U** and **V**; $n = 4$–6 per group in **D**; $n = 5$–6 per group in **L–O**; $n = 3$–4 per group in **K** and **P**). $P < 0.05$ was considered a significant difference; ns, no significance (one-way ANOVA with Holm-Sidak multiple comparison tests). **, $P < 0.01$; ***, $P < 0.001$. Scale bar, 100 μm. FMO, fluorescence minus one; SN, supernatants. (**Q,** Created with BioRender.com.)

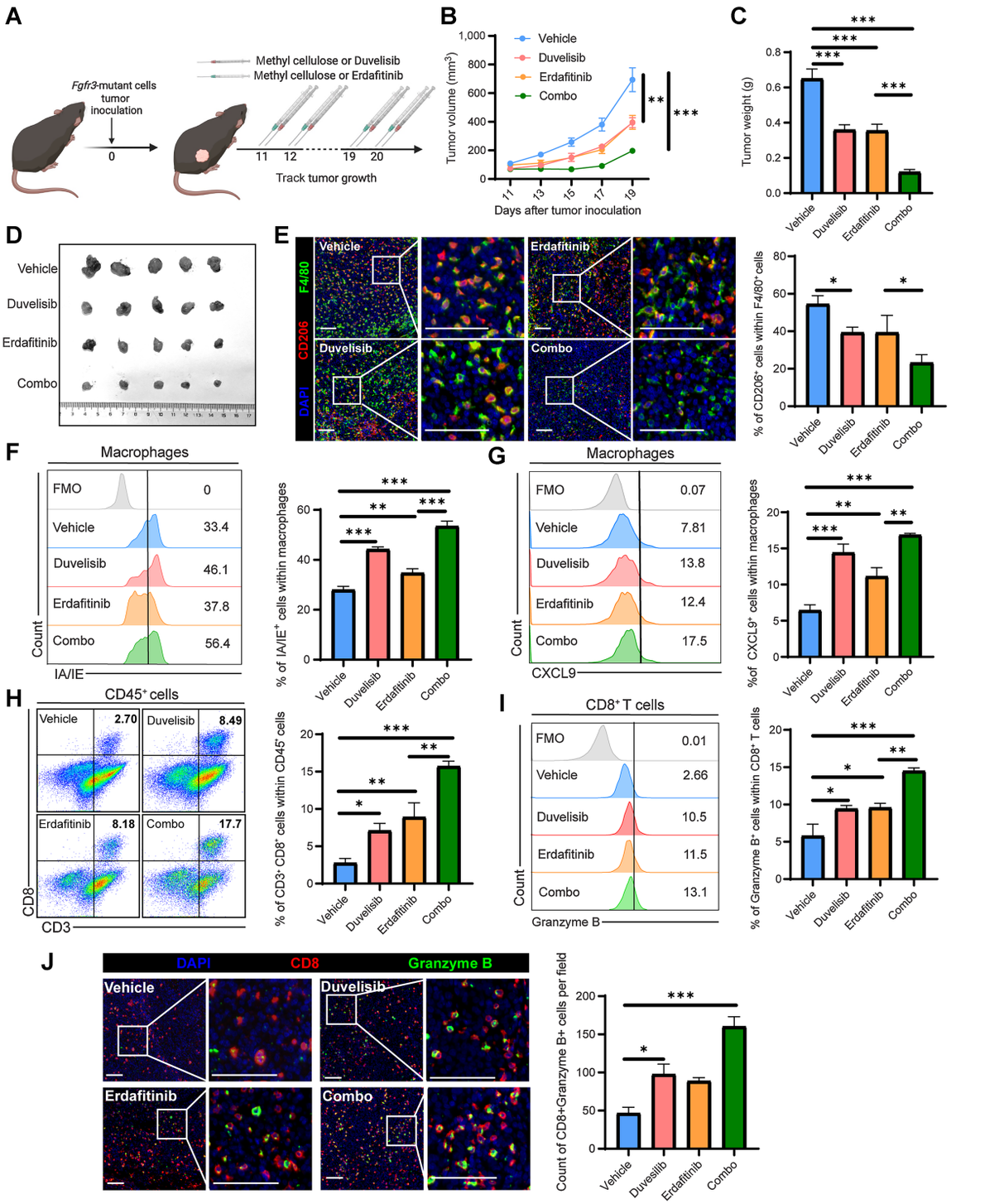

Figure 6.

Duvelisib augments the antitumor efficacy of erdafitinib in combination therapy. **A,** Schematic illustration of duvelisib and erdafitinib treatment strategy. **B** and **C,** Tumor growth curves (**B**) and tumor weights (**C**) of the groups receiving vehicle, duvelisib, erdafitinib, and combination therapy, respectively. **D,** Images of the dissected tumors from mice in the vehicle, duvelisib, erdafitinib, and combination treatment groups. **E,** Representative images and statistical analysis show $CD206^+$ $F4/80^+$ cell infiltration in the indicated groups. **F** and **G,** Flow cytometry analysis and statistical analysis illustrating the proportion of IA/IE^+ cells (**F**) and $CXCL9^+$ cells (**G**) within macrophages in the indicated groups. **H** and **I,** Flow cytometry analysis illustrating the proportion of $CD3^+CD8^+$ cells within $CD45^+$ cells (**H**) and the proportion of granzyme B^+ cells within $CD8^+$ T cells (**I**) in the indicated groups. **J,** Representative images and statistical analysis show $CD8^+$ granzyme B^+ cell infiltration in the indicated groups. The data are shown as the mean ± SEM values ($n = 5$ per group in **B–D**; $n = 4$–5 per group in **F–I**; $n = 3$–4 per group in **E** and **J**). $P < 0.05$ was considered a significant difference (one-way ANOVA with Holm-Sidak multiple comparison tests). *, $P < 0.05$; **, $P < 0.01$; ***, $P < 0.001$. Scale bar, white, 100 μm. (**A,** Created with BioRender.com.)

Authors' Disclosures

W. Zhong reports grants from National Natural Science Foundation of China and Natural Science Foundation of Guangdong during the conduct of the study. T. Lin reports grants from National Natural Science Foundation of China and Key Areas Research and Development Program of Guangdong during the conduct of the study. J. Huang reports grants from National Natural Science Foundation of China during the conduct of the study. No disclosures were reported by the other authors.

Authors' Contributions

Y. Ouyang: Conceptualization, formal analysis, validation, investigation, visualization, methodology, writing–original draft, writing–review and editing. **Z. Ou:** Conceptualization, investigation, methodology, writing–original draft. **W. Zhong:** Conceptualization, formal analysis, writing–original draft, writing–review and editing. **J. Yang:** Investigation. **S. Fu:** Resources, validation, investigation. **N. Ouyang:** Resources, validation, investigation. **J. Chen:** Methodology. **L. Xu:** Methodology. **D. Wu:** Investigation. **J. Qian:** Investigation. **Y. Lin:** Software. **T. Lin:** Supervision, writing–review and editing. **J. Huang:** Supervision, writing–review and editing.

Acknowledgments

This study was supported by the National Natural Science Foundation of China (grant no. 81825016 to Tianxin Lin; 81F961128027 to J. Huang; and 82373254 to Wenlong Zhong), Natural Science Foundation of Guangdong (grant no. 2023A1515010258 to W. Zhong), and Key Areas Research and Development Program of Guangdong (grant no. 2018B010109006 to T. Lin). The authors would like to thank Prof. Phei Er Saw for her advice on the experimental design.

The publication costs of this article were defrayed in part by the payment of publication fees. Therefore, and solely to indicate this fact, this article is hereby marked "advertisement" in accordance with 18 USC section 1734.

Note

Supplementary data for this article are available at Cancer Research Online (http://cancerres.aacrjournals.org/).

Received April 8, 2023; revised July 31, 2023; accepted September 26, 2023; published first September 28, 2023.

References

1. Siegel RL, Miller KD, Fuchs HE, Jemal A. Cancer statistics, 2022. CA Cancer J Clin 2022;72:7–33.
2. Cathomas R, Lorch A, Bruins HM, Comperat EM, Cowan NC, Efstathiou JA, et al. The 2021 updated European Association of Urology guidelines on metastatic urothelial carcinoma. Eur Urol 2022;81:95–103.
3. Robertson AG, Kim J, Al-Ahmadie H, Bellmunt J, Guo G, Cherniack AD, et al. Comprehensive molecular characterization of muscle-invasive bladder cancer. Cell 2018;174:1033.
4. Pietzak EJ, Bagrodia A, Cha EK, Drill EN, Iyer G, Isharwal S, et al. Next-generation sequencing of nonmuscle invasive bladder cancer reveals potential biomarkers and rational therapeutic targets. Eur Urol 2017;72:952–9.
5. Teo MY, Mota JM, Whiting KA, Li HA, Funt SA, Lee CH, et al. Fibroblast growth factor receptor 3 alteration status is associated with differential sensitivity to platinum-based chemotherapy in locally advanced and metastatic urothelial carcinoma. Eur Urol 2020;78:907–15.
6. Helsten T, Elkin S, Arthur E, Tomson BN, Carter J, Kurzrock R. The FGFR landscape in cancer: analysis of 4,853 tumors by next-generation sequencing. Clin Cancer Res 2016;22:259–67.
7. Loriot Y, Necchi A, Park SH, Garcia-Donas J, Huddart R, Burgess E, et al. Erdafitinib in locally advanced or metastatic urothelial carcinoma. N Engl J Med 2019;381:338–48.
8. Turner N, Grose R. Fibroblast growth factor signalling: from development to cancer. Nat Rev Cancer 2010;10:116–29.
9. Robertson AG, Kim J, Al-Ahmadie H, Bellmunt J, Guo G, Cherniack AD, et al. Comprehensive molecular characterization of muscle-invasive bladder cancer. Cell 2017;171:540–56.
10. Kamoun A, de Reynies A, Allory Y, Sjodahl G, Robertson AG, Seiler R, et al. A consensus molecular classification of muscle-invasive bladder cancer. Eur Urol 2020;77:420–33.
11. Foth M, Ismail NFB, Kung JSC, Tomlinson D, Knowles MA, Eriksson P, et al. FGFR3 mutation increases bladder tumourigenesis by suppressing acute inflammation. J Pathol 2018;246:331–43.
12. Hu Y, Lu Y, Xing F, Hsu W. FGFR1/MAPK-directed brachyury activation drives PD-L1-mediated immune evasion to promote lung cancer progression. Cancer Lett 2022;547:215867.
13. Li P, Huang T, Zou Q, Liu D, Wang Y, Tan X, et al. FGFR2 promotes expression of PD-L1 in colorectal cancer via the JAK/STAT3 signaling pathway. J Immunol 2019;202:3065–75.
14. Lu M, Wang K, Ji W, Yu Y, Li Z, Xia W, et al. FGFR1 promotes tumor immune evasion via YAP-mediated PD-L1 expression upregulation in lung squamous cell carcinoma. Cell Immunol 2022;379:104577.
15. Faubert B, Solmonson A, DeBerardinis RJ. Metabolic reprogramming and cancer progression. Science 2020;368:eaaw5473.
16. Jin N, Bi A, Lan X, Xu J, Wang X, Liu Y, et al. Identification of metabolic vulnerabilities of receptor tyrosine kinases-driven cancer. Nat Commun 2019;10:2701.
17. Liberti MV, Locasale JW. The warburg effect: how does it benefit cancer cells? Trends Biochem Sci 2016;41:211–8.
18. Amelio I, Cutruzzola F, Antonov A, Agostini M, Melino G. Serine and glycine metabolism in cancer. Trends Biochem Sci 2014;39:191–8.
19. Geeraerts SL, Heylen E, De Keersmaecker K, Kampen KR. The ins and outs of serine and glycine metabolism in cancer. Nat Metab 2021;3:131–41.
20. He F, Yin Z, Wu C, Xia Y, Wu M, Li P, et al. l-Serine lowers the inflammatory responses during pasteurella multocida infection. Infect Immun 2019;87:e00677–19.
21. Wilson JL, Nagele T, Linke M, Demel F, Fritsch SD, Mayr HK, et al. Inverse data-driven modeling and multiomics analysis reveals PHGDH as a metabolic checkpoint of macrophage polarization and proliferation. Cell Rep 2020;30:1542–52.
22. Hao Y, Hao S, Andersen-Nissen E, Mauck WM 3rd, Zheng S, Butler A, et al. Integrated analysis of multimodal single-cell data. Cell 2021;184:3573–87.
23. Haghverdi L, Lun ATL, Morgan MD, Marioni JC. Batch effects in single-cell RNA-sequencing data are corrected by matching mutual nearest neighbors. Nat Biotechnol 2018;36:421–7.
24. Mariathasan S, Turley SJ, Nickles D, Castiglioni A, Yuen K, Wang Y, et al. TGFbeta attenuates tumour response to PD-L1 blockade by contributing to exclusion of T cells. Nature 2018;554:544–8.
25. Rosenberg JE, Hoffman-Censits J, Powles T, van der Heijden MS, Balar AV, Necchi A, et al. Atezolizumab in patients with locally advanced and metastatic urothelial carcinoma who have progressed following treatment with platinum-based chemotherapy: a single-arm, multicentre, phase 2 trial. Lancet 2016;387:1909–20.
26. Jin S, Guerrero-Juarez CF, Zhang L, Chang I, Ramos R, Kuan CH, et al. Inference and analysis of cell-cell communication using CellChat. Nat Commun 2021;12:1088.
27. Yadav V, Zhang X, Liu J, Estrem S, Li S, Gong XQ, et al. Reactivation of mitogen-activated protein kinase (MAPK) pathway by FGF receptor 3 (FGFR3)/Ras mediates resistance to vemurafenib in human B-RAF V600E mutant melanoma. J Biol Chem 2012;287:28087–98.
28. Lawrence T, Natoli G. Transcriptional regulation of macrophage polarization: enabling diversity with identity. Nat Rev Immunol 2011;11:750–61.
29. Kerneur C, Cano CE, Olive D. Major pathways involved in macrophage polarization in cancer. Front Immunol 2022;13:1026954.
30. Kaneda MM, Messer KS, Ralainirina N, Li H, Leem CJ, Gorjestani S, et al. PI3Kgamma is a molecular switch that controls immune suppression. Nature 2016;539:437–42.
31. Liu X, Zhang W, Xu Y, Xu X, Jiang Q, Ruan J, et al. Targeting PI3Kgamma/AKT pathway remodels LC3-associated phagocytosis induced immunosuppression after radiofrequency ablation. Adv Sci 2022;9:e2102182.
32. Goossens P, Rodriguez-Vita J, Etzerodt A, Masse M, Rastoin O, Gouirand V, et al. Membrane cholesterol efflux drives tumor-associated macrophage reprogramming and tumor progression. Cell Metab 2019;29:1376–89.
33. Flinn IW, O'Brien S, Kahl B, Patel M, Oki Y, Foss FF, et al. Duvelisib, a novel oral dual inhibitor of PI3K-delta, gamma, is clinically active in advanced hematologic malignancies. Blood 2018;131:877–87.

34. Schuler M, Cho BC, Sayehli CM, Navarro A, Soo RA, Richly H, et al. Rogaratinib in patients with advanced cancers selected by FGFR mRNA expression: a phase 1 dose-escalation and dose-expansion study. Lancet Oncol 2019;20:1454–66.
35. Jing W, Wang G, Cui Z, Xiong G, Jiang X, Li Y, et al. FGFR3 destabilizes PD-L1 via NEDD4 to control T-cell-mediated bladder cancer immune surveillance. Cancer Res 2022;82:114–29.
36. Vazquez A, Liu J, Zhou Y, Oltvai ZN. Catabolic efficiency of aerobic glycolysis: the warburg effect revisited. BMC Syst Biol 2010;4:58.
37. Levy P, Bartosch B. Metabolic reprogramming: a hallmark of viral oncogenesis. Oncogene 2016;35:4155–64.
38. Ratnikov BI, Scott DA, Osterman AL, Smith JW, Ronai ZA. Metabolic rewiring in melanoma. Oncogene 2017;36:147–57.
39. Yang M, Vousden KH. Serine and one-carbon metabolism in cancer. Nat Rev Cancer 2016;16:650–62.
40. Locasale JW. Serine, glycine and one-carbon units: cancer metabolism in full circle. Nat Rev Cancer 2013;13:572–83.
41. Leone RD, Powell JD. Metabolism of immune cells in cancer. Nat Rev Cancer 2020;20:516–31.
42. Ma EH, Bantug G, Griss T, Condotta S, Johnson RM, Samborska B, et al. Serine is an essential metabolite for effector T cell expansion. Cell Metab 2017;25:345–57.
43. Xia L, Oyang L, Lin J, Tan S, Han Y, Wu N, et al. The cancer metabolic reprogramming and immune response. Mol Cancer 2021;20:28.
44. Shan X, Hu P, Ni L, Shen L, Zhang Y, Ji Z, et al. Serine metabolism orchestrates macrophage polarization by regulating the IGF1-p38 axis. Cell Mol Immunol 2022;19:1263–78.
45. Rodriguez AE, Ducker GS, Billingham LK, Martinez CA, Mainolfi N, Suri V, et al. Serine metabolism supports macrophage IL-1beta production. Cell Metab 2019;29:1003–11.
46. Hoxhaj G, Manning BD. The PI3K-AKT network at the interface of oncogenic signalling and cancer metabolism. Nat Rev Cancer 2020;20:74–88.
47. Guo J, Wei W. Fine-tuning AKT kinase activity through direct lysine methylation. Cell Cycle 2019;18:917–22.
48. Chan CH, Jo U, Kohrman A, Rezaeian AH, Chou PC, Logothetis C, et al. Posttranslational regulation of Akt in human cancer. Cell Biosci 2014;4:59.
49. Manning BD, Toker A. AKT/PKB signaling: navigating the network. Cell 2017;169:381–405.
50. Guo J, Dai X, Laurent B, Zheng N, Gan W, Zhang J, et al. AKT methylation by SETDB1 promotes AKT kinase activity and oncogenic functions. Nat Cell Biol 2019;21:226–37.
51. Wang G, Long J, Gao Y, Zhang W, Han F, Xu C, et al. SETDB1-mediated methylation of Akt promotes its K63-linked ubiquitination and activation leading to tumorigenesis. Nat Cell Biol 2019;21:214–25.
52. Bilanges B, Posor Y, Vanhaesebroeck B. PI3K isoforms in cell signalling and vesicle trafficking. Nat Rev Mol Cell Biol 2019;20:515–34.
53. Vanhaesebroeck B, Perry MWD, Brown JR, Andre F, Okkenhaug K. PI3K inhibitors are finally coming of age. Nat Rev Drug Discov 2021;20:741–69.
54. Curigliano G, Shah RR. Safety and tolerability of phosphatidylinositol-3-kinase (PI3K) inhibitors in oncology. Drug Saf 2019;42:247–62.